

Hazomes: Earth’s natural multi-hazard terrestrial disturbance regimes

Non-peer reviewed preprint submitted to EarthArXiv

Chahan M. Kropf^{1,2*}, Sarah Hülsen^{1,2}, Zélie Stalhandske^{1,2},
Stijn Hantson³, Philip J. Ward^{4,5}, Marthe Wens⁴, Nadav Peleg^{6,7},
David N. Bresch^{1,2}, Carmen B. Steinmann^{1,2}

¹Institute for Environmental Decisions, ETH Zurich, Zurich, Switzerland

²Federal Office of Meteorology and Climatology MeteoSwiss, Zurich-Airport, Switzerland

³School of Sciences and Engineering, Universidad del Rosario, Bogotá, Colombia

⁴Institute for Environmental Studies, Vrije Universiteit Amsterdam, Amsterdam, the Netherlands

⁵Deltares, Delft, the Netherlands

⁶Institute of Earth Surface Dynamics, University of Lausanne, Lausanne, Switzerland

⁷Expertise Center for Climate Extremes, University of Lausanne, Lausanne, Switzerland

*Corresponding author. Email: ckropf@ethz.ch

Ecosystems and societies have evolved together and are shaped by local natural hazard regimes. We introduce hazomes, an Earth classification based on multi-hazard disturbance patterns. By combining open-source intensity and return period data for eight hazard types, we identify thousands of distinct terrestrial disturbance regimes. Hazomes aims to deepen insight into ecosystem and societal resilience, enabling research on how ecological and human systems have evolved under specific hazard regimes and how they may be threatened by climate change. Using two complexity-diversity metrics, we demonstrate that hazomes provide insights beyond climate zones or biomes. Moreover, we show how distant cities can belong to the same hazome, serving as hazard disturbance analogues for shared adaptation strategies. This approach complements existing multi-hazard assessments by shifting the focus from individual events to disturbance regimes, better reflecting long-term societal adaptation and ecosystem resilience.

1 Introduction

Natural hazards, such as earthquakes, tropical storms, and droughts, play a fundamental role in shaping human and natural systems (1). For decades, scientists have studied individual hazards, examining their drivers, intensity (also referred to as magnitudes or severity depending on the

context), return period (equivalent to the inverse of the frequency), and consequences (2). More recently, a growing body of research has shifted toward an interdisciplinary perspective, recognising that the interaction between multiple hazards can amplify risks through compounding and cascading effects (3,4). The United Nations Office for Disaster Risk Reduction (UNDRR) and the International Science Council (ISC) published in 2025 the updated Hazard Information Profiles (HIPs) (5) to provide a systematic common set of (multi-) hazard definitions. However, a comprehensive classification of Earth's regions based on the intensity and frequency characteristics of multiple natural hazards is currently lacking, despite the availability of global datasets for individual hazards (6). We introduce the concept of *hazomes*, a framework that systematically classifies regions by their unique multi-hazard disturbance regimes, considering their types, return periods, and intensities.

The idea of classifying Earth's regions based on shared characteristics is well-established, dating back at least to the early 19th-century and Alexander von Humboldt's work on vegetation and climate zones (7). Well-known examples include climate zones, biomes, and ecoregions (8, 9, 10, 11, 12). Climate zones, such as those in the Köppen-Geiger classification (13, 14), are based on regional differences in seasonal temperature and precipitation. Biomes extend this concept by characterising large ecological communities primarily by climate and dominant vegetation (12, 15), while ecoregions provide a more detailed classification, considering factors such as climate, soil, and species composition (16, 17). Although climate-based classification systems have often been successful in separating different forest ecoregions, recent research showed that multiple non-forest ecosystems cannot be predicted based on these abiotic factors; instead, they are shaped by their disturbance regime (18, 19, 20).

In the field of risk science, the recognition of the limitations of single-hazard analysis has led to a shift towards studying multi-hazard risks (21, 22, 3, 4, 23, 24, 25, 26). Research has demonstrated how hazards interact in various ways, such as cascading disasters, where one hazard triggers another (e.g., storm lightning that triggers wildfires) (27), and compounding events, where multiple hazards occur simultaneously or sequentially, amplifying impacts (e.g., intensified floods after a drought period) (24). However, integrating different types of hazards into a unified risk assessment framework remains a challenge due to their diverse characteristics (5).

Here we combine global terrestrial maps of intensity distributions for different return periods of eight major hazard types, and define two intensity thresholds for each type. Combining these maps and thresholds, we define *hazomes*: global natural multi-hazard terrestrial disturbance regimes. Our definition is based on the understanding that ecosystems and human systems within a *hazome* adapt to their specific combination of multi-hazard intensity and return period profiles, similar to how organisms in biomes adapt to environmental conditions. For example, small trees with deep roots can thrive in environments with extreme wind and a high water deficit; and dams may be built to protect against floods while also being able to withstand earthquakes (28, 29). With this work, our aim is to enable insights into ecosystem and societal resilience, guiding effective risk management and resilience strategies across diverse regions with a multi-hazard perspective, reducing maladaptation, and enhancing our capacity to mitigate the impacts of natural hazards on both natural and societal systems.

2 Hazomes

Our classification of Earth’s land into hazomes (see Fig. 1) includes eight types of natural hazards, selected based on two main criteria: 1) the hazard should not be confined to a specific region (e.g., tornadoes in North America) or a small area (e.g., landslides), and 2) should be generically relevant in terms of impacts on societies and ecosystems (see Methods 4). Following these considerations,

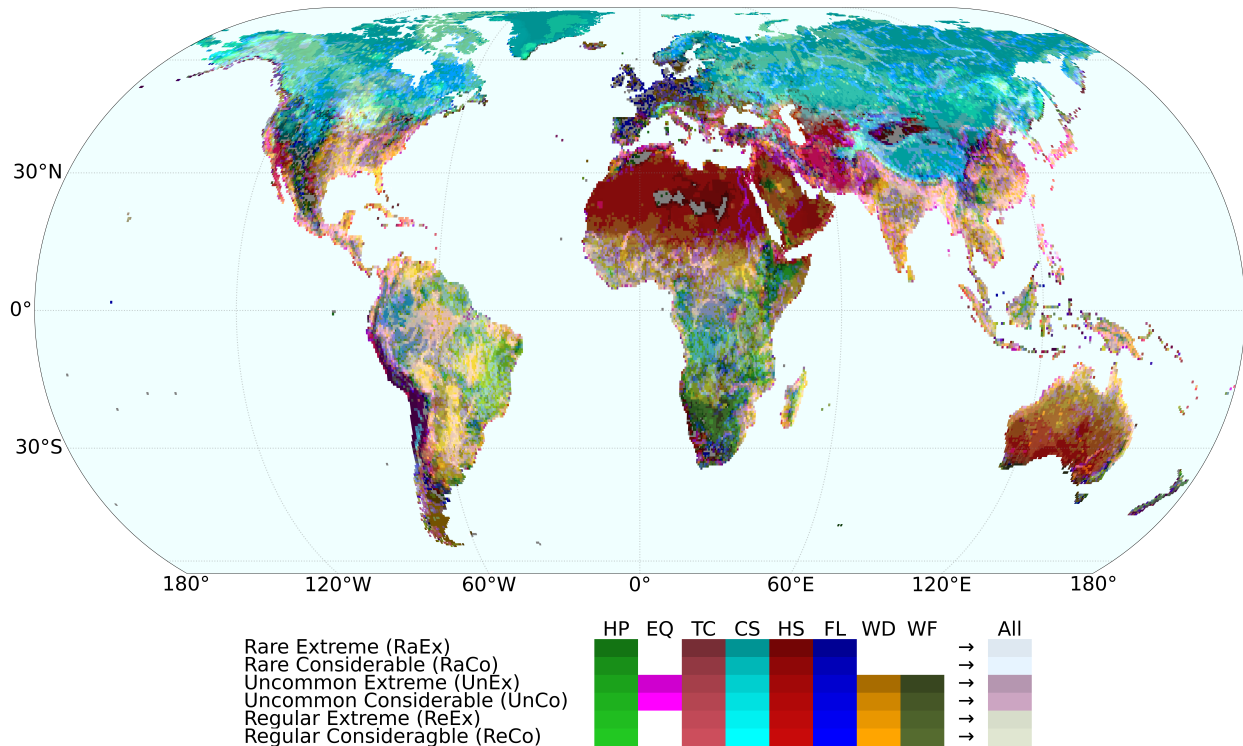


Figure 1: Global hazomes map. The included hazard types are heavy precipitation (HP), earthquakes (EQ), tropical cyclones (TC), cold stress (CS), heat stress (HS), coastal and river floods (FL), water deficit (WD), and wildfires (WF). There are 3 return periods (Re: regular; Un: uncommon; Ra: rare) and 2 intensity (Co: considerable; Ex: extreme) thresholds (see Tab. 1). All combinations of hazard type, intensity thresholds, and return periods are in principle possible. In practice, we obtain 8046 different combinations, i.e., hazomes, on land globally. The colour shading of each hazard type goes from rare-extreme (dark) to regular-considerable (light). The colour of a grid cell is the additive mixing (as for light, more colours mix to more white) of the colours of the corresponding hazome. We note that the colour is not always intuitive to interpret visually, and distinct hazomes might have very similar colours (e.g., rare-extreme floods (dark blue) with regular-considerable heat stress (light red) mixes to light magenta, similar to regular-considerable earthquakes). All hazomes colours are shown in the supplementary figure S4. Since it is not possible to find a unique colour combination for all 8046 hazomes, an interactive map is available online for more detailed exploration.

we include heavy precipitation (HP), earthquakes (EQ), tropical cyclones (TC), cold stress (CS), heat stress (HS), coastal and river floods (FL), temporary water deficit (drought; WD), and wildfires (WF). For each type of hazard, we deploy return period maps on land at a spatial resolution of 0.5° ,

which entail the expected intensity at given return periods for each grid cell. For each hazard type we define *regular* (Re; < 5 – 10 years), *uncommon* (Un; < 20 – 25 years) and *rare* (Ra; < 100 years) return period (i.e., inverse annual occurrence probability) intensity maps if the data is available (Table 1). We then split these maps into two intensity categories, representing grid cells subject to at least *considerable* (Co) or *extreme* (Ex) intensities (Table 1).

Each type of hazard is described in terms of one absolute intensity variable (e.g., flood depth in metres) and corresponding intensity categories (e.g., Co: > 0.3m and Ex:> 1.5m) (Table 1). Although many studies employ relative values to capture the varying “extremeness” and the potential resulting impact at a given intensity on ecosystems and societies, we favour absolute values to ensure global consistency. This allows us to compare regions across the world and contextualise the occurrence of multiple hazards. For instance, in Zurich (Switzerland), uncommon extreme water deficits are coupled with rare considerable floods, while in Bengaluru (India), regular extreme water deficits are paired with regular considerable heavy precipitations and regular considerable heat stress.

Hazomes are obtained by overlaying the maps of all types of hazards for regular, uncommon, and rare return periods at considerable and extreme intensity. Then each grid cell is assigned the most frequent and most extreme value for each hazard type 4. Globally, this yields 8046 hazomes, i.e., unique combinations of hazard type, return period, and intensity, shown in Figure 1 (see Methods for the hazome name coding convention 4). We find that while there is a certain latitude pattern similar to the climate zones (13, 14), the distribution of hazomes is complex, with several longitudinal and regional patterns emerging. In particular, while the distribution patterns of the individual hazards (c.f. figures S5, S8-S15) may be familiar, the combinations of all hazard types are less intuitive. A series of online interactive maps allows the reader to explore the hazomes further, providing a rich set of information. For the visual maps, we assign a base colour to each hazard type and different shades for intensity and return period. A grid cell is coloured with the additive mix (similar to light mixing, more colours mix to more white) of all combinations of hazard type, intensity, and return period. As colour mixing is not always intuitive, distinct hazomes may appear visually similar (e.g., floods and heat stress mixing into light magenta, resembling the colour for earthquakes), with all colours listed in supplementary Figure S4.

Hazomes show an intricate pattern of hazard type diversity, with generally a higher number of hazard types in tropical regions compared to extra-tropical regions (Fig. 2a). Regions with low hazard diversity include climates that can broadly be considered difficult to sustain life, such as deserts, high mountain plateaus, or the tundra. For example, deserts such as the Sahara are hot and arid on average, but are not subject to many extreme deviations and are not affected by many other hazards. In addition, north-west Europe has a comparatively low hazard diversity, with most areas being affected by no hazard or only by either water deficit or flood. No terrestrial grid cell has more than six of the eight hazard types.

2.1 Hazome metrics

To capture not only the diversity of hazards, but also their intensity and return period, we derive the haz-score metric, presented in Fig. 2 b). It is defined as the sum of hazard types that exceed intensity thresholds for each return period (see Methods 4). The haz-score is higher the more intense, the more frequent, and the more diverse a hazome is. Regions with low haz-scores (below 3) are mostly regions with low diversity of hazards (below 2). Medium haz-scores (between 8-14) are found

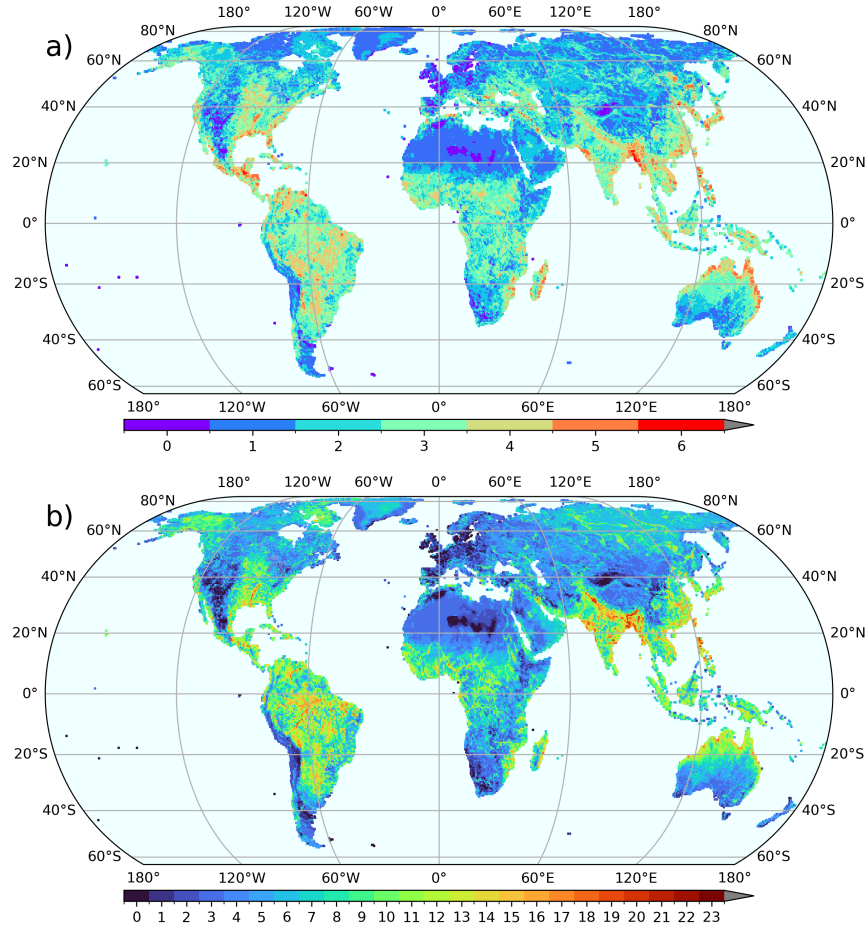


Figure 2: Hazome metric maps. a) Map counting the number of different hazard types in each hazome. Note that no grid cell has more than 6 different hazard types out of a possible maximum of 8. b) Haz-score obtained as the sum of all return periods and intensities for all hazards (see Methods 4 for details). Higher haz-score values indicate higher diversity of hazards, higher severity and lower return period (higher frequency). Interactive maps are available online for more detailed exploration.

both in regions with several hazard types (4-5) at lower intensity and higher return period (lower frequency) (e.g., Vietnam and Japan) and in regions with fewer hazard types (2-3) at higher intensity and lower return period (higher frequency) (e.g., Central and West Africa). The highest haz-score is found in the delta region of the Ganges and Brahmaputra rivers in Bangladesh (haz-score of up to 23), where up to six hazards (EQ, HP, TC, WD, FL, HS) occur with high intensity and low return period (high frequency). Generally speaking, large river systems are associated with a high haz-scores on all continents (haz-score above 14), such as the Amazon, the Congo, the Ganges, the Indus, the Brahmaputra, the Mississippi, or the Yangtze.

The haz-score can be contrasted with bio-climatic and societal classifications. The median value for (a) ecoregions, (b) climate zones, (c) countries, and (d) biomes is available online as interactive maps and discussed in the supplementary material 5. Moreover, the number of distinct hazomes present per (a) ecoregion, (b) climate zones, (c) countries (administrative regions), and (d) biomes

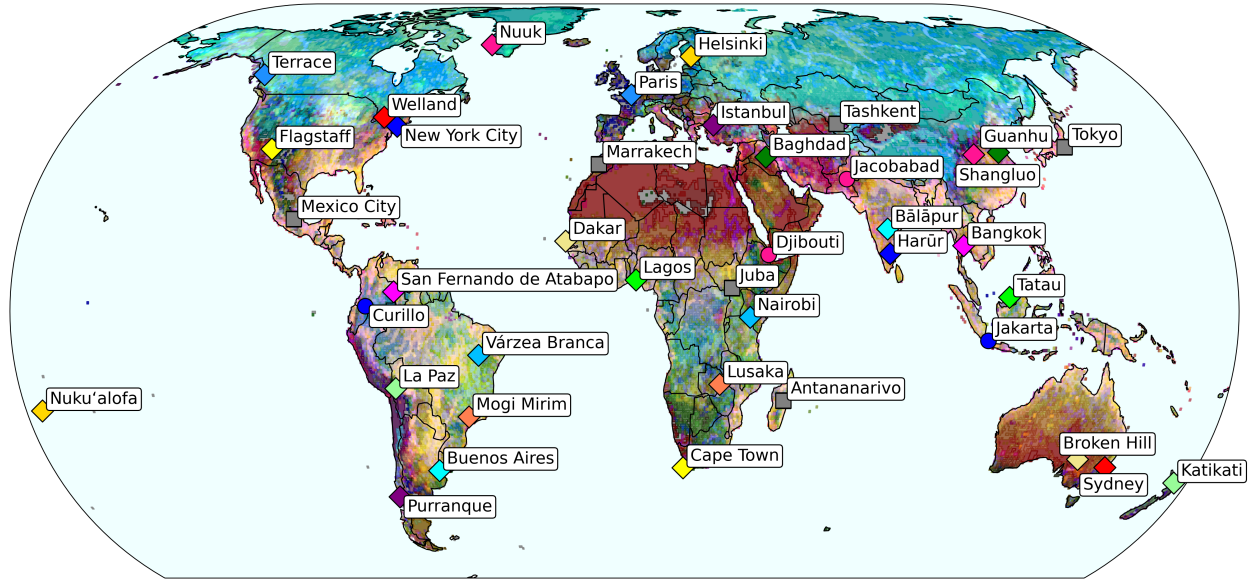


Figure 3: Hazome twin cities map. City pairs that share the same hazome and are at least 5 degrees distant from one another are shown with the same marker and colour. Cities with gray square markers (Tokyo, Tashkent, Antananarivo, Juba, and Mexico City) have no hazome twin at least 5 degrees distant. City pairs marked by circles are in the same climate zones (Curillo-Jakarta, Jacobabad-Djibouti). City pairs marked with diamonds are in different climate zones. The cities shown were selected randomly to represent a large diversity of global regions. An interactive map is available online for exploring all city twins above 5000 inhabitants.

is shown online and discussed in the supplementary material 5.

2.2 Hazomes for adaptation

Over time, societies have adapted to their regional hazome with different strategies to become more resilient to these specific combinations of hazard types, intensities, and return periods (30). For example, building a river flood wall in an earthquake-prone region requires specific engineering approaches that may be distinct from a region with extreme heavy precipitation (31). Using hazomes, regions with similar disturbance regimes, as shown in Fig. 3, can be identified to reveal a rich network of learning opportunities (31).

To illustrate, we randomly selected several large known cities to cover most regions of the world and then assigned the most distant (at least 5 degrees away), largest city with the same hazome. We show some distant pairings, such as Dakar (Senegal) and Broken Hill (Australia), or La Paz (Bolivia) and Katikati (New Zealand). Some pairs of cities are located in the same climate zones, while the other pairs are in different climates (see also Fig. S6), and some cities do not have an exact hazome twin that is at least 5° distant. An interactive map is available online to explore all twin cities with over 5000 inhabitants.

3 Discussion

Hazomes provide a global perspective on natural multi-hazard terrestrial disturbance regimes that can serve as a foundation for global multi-hazard risk assessment, climate risk management, ecosystem restoration, and contribute to both natural and societal resilience. The new classification complements existing climate classification schemes with the inclusion of extreme weather patterns and other natural hazards.

Hazomes represent hazards, not risk; risk arises only when hazards impact exposed and vulnerable systems (32). For human societies, the United Nations Office for Disaster Risk Reduction (UNDRR) further defines risk to include the capacity of societies to respond (33). Hence, the same hazard intensity represents very different risks in societies with different vulnerabilities and response capacities. For instance, earthquake-resistant buildings in Japan might not be strongly damaged by moderate earthquakes, while non-resistant buildings in regions with less frequent earthquakes or less coping capacity could incur important damage. Thus, hazomes, defined with globally consistent fixed intensity thresholds, may describe very different risks locally. This is no different than for average climate conditions, where, for example, 10°C would represent unprecedented cold weather in a hot and humid country like Singapore, but would be a warm winter day in Finland. Bearing in mind the difference between hazard and risk, hazomes provide the basis for broad applications.

In humanitarian emergency contexts, understanding typical regional multi-hazard distributions may support improved response planning to enable faster and more effective mobilisation of resources during crises (34). For example, floods in a tropical cyclone area might require different intervention plans than in a cold stress area. For climate adaptation planning, hazomes may support the design of large-scale adaptation strategies, avoiding potential maladaptation resulting from single-hazard planning (35). For example, adaptation measures at the building-level against floods and earthquakes might have conflicting effects (35). The identification of regions with similar hazard disturbance regimes, which can thus serve as effective analogues, allows adaptation strategies to be shared and refined based on successes and lessons learnt. In addition, hazomes could also be used to explore inequalities in hazard exposure (36) and possible social implications to strengthen just adaptation planning. In financial risk management, it enables organising regions based on shared hazard characteristics, supporting the design of multi-hazard financial reporting and instruments (37), offering a pathway to global risk pooling (38).

For ecosystem management and restoration, knowledge of disturbance regimes is needed to inform sustainable practices and improve the resilience of local ecosystems. By tailoring ecosystem management to the specific multi-hazard profile, one can support biodiversity, enhance ecosystem services, and promote sustainable land use (39, 40, 41). Disturbance regimes may also be relevant when evaluating the long-term viability of carbon offset credits that are often assigned to sensitive ecosystems subject to multiple disturbances (42, 43). Although high natural disturbances are not per-se negative for ecosystems, they might affect their dynamics and lead to large carbon storage capacity fluctuations that should be taken into account when pricing credits and projecting their contributions to emission compensation.

Hazomes can inform the development and refinement of ecological models, such as species distribution models. These models, which predict where species may thrive under specific environmental conditions, would benefit from integrating multi-hazard disturbance regimes shaping interconnected species networks. Although large scale ecological disturbance studies where mul-

multiple hazards are considered jointly are still limited, it was already shown that considering these can result in unexpected disturbance behaviour, regime shifts, and non-linear changes in ecosystem structures (44, 45). More generally speaking, global multi-hazard profiles can help the systematic study of how ecosystems and their web of species (e.g., fungi, plants, insects, birds, and mammals) are vulnerable, resilient, or dependent on natural perturbation regimes (46, 19). This could help identify suitable locations for ecosystem restoration by highlighting regions with similar disturbance patterns, offering information on effective strategies for habitat restoration and species reintroduction.

Defining hazomes required methodological choices, including hazard type selection, metric definition, and thresholding, all of which strongly influence the resulting classification. To ensure stability and global consistency, we fixed thresholds for intensity and return periods rather than relying on unstable clustering approaches (see Methods 4). Our sensitivity analysis (see the supplementary material 5) shows that the choice of thresholds influences the grid cell level and area distribution of the hazards profiles, with the highest sensitivity to the extreme intensity thresholds of cold and heat stress, as well as the considerable intensity thresholds of floods and heavy precipitation. Hence, hazomes with these categories are to be interpreted with care. We note that each type of natural hazard was reduced to a single intensity variable, which cannot capture all dimensions of its effects. For instance, tropical cyclones are represented by wind speed only, thus not characterising heavy precipitation, storm surges, landslides, salinity intrusion, etc. While some of these are partially covered by other data (coastal floods and heavy precipitation), others are completely absent. Although incomplete, this macro-scale hazard depiction that does not resolve all sub-hazard components is still common in the impact assessment research and practice community (6, 32). Furthermore, by representing hazards only through annual return periods, we do not account for seasonality, sub-annual frequencies, or the co-occurrence, cascading, and compounding of hazard events (27, 6). Finally, we note that the data for each hazard type come from a different source, which required regriding to a common resolution and resulted in certain inconsistencies in the definition of complex coastal zones and small islands.

The concept of hazomes allows for many extensions and refinements adapted to a diversity of use cases. Hazomes would benefit from extending the hazard data sets to have intensity estimates for all return periods. We are currently missing values for the water deficit and wildfires, which were derived from historical data, and for which the extrapolation method is yet unclear. Hazomes were derived from a past, yet rapidly changing climate. For example, extreme precipitation is rapidly intensifying with rising temperatures, and its statistical characteristics could differ considerably from those observed today for some locations already within the next decade (47). Hence, it would be beneficial to derive maps of projected time periods in the future to depict the evolution of hazomes with climate change. Moreover, for adaptation and mitigation strategy guidance, an important next step is to increase the resolution of hazomes. As this might be difficult to do at a global level, one might aim for regional hazome maps instead. A higher resolution would also naturally lead to the inclusion of a larger diversity of hazards, including more localised ones such as volcanoes, tsunamis, landslides, tornados, sand storms, derechos, convective and extra-tropical storms. Specialised high-resolution hazomes can also be derived for specific sectors such as agriculture and energy. Finally, it would also be useful to extend the hazomes to aquatic systems to describe important hazards such as marine heat waves or eutrophication events.

In an increasingly interconnected and hazard-prone world, hazomes offer a foundational framework for understanding and managing global natural multi-hazard disturbance regimes, providing

a vital tool for building resilience and informing sustainable decisions across social-ecological systems.

4 Methods

The selection of hazard data is a critical step in defining the hazomes. The process, while based on a certain level of subjectivity as any map categorisation exercise, was guided by clear criteria: 1. The data set must be open source and available since we want the hazomes to be transparent, reproducible, and free to use for anyone; 2. The hazard should be relevant on a global scale to allow a consistent world categorisation, meaning we excluded regional hazard types such as tornadoes or small-scale hazards such as landslides; and 3. The hazard intensity variable must allow for globally consistent comparison and should not focus on one particular impact. The final criterion is crucial and might run contrary to established conventions in specialised fields. This is on purpose, as the hazomes are meant to be a globally consistent tool for comparison across regions and across as many fields of application as possible. The final selection of the data set was done in cooperation with experts in the field of each of the hazards. Note that all hazards for which the original dataset was not at the hazomes' regular grid of 0.5° resolution (totalling 85710 grid cells on land) were regridded. Detailed descriptions of the chosen datasets and applied transformations are given below for each hazard separately.

To reduce complexity while keeping a maximum of information, we converged to the choice of 3 return periods per hazard – regular (Re) ($< 5 - 10$ years), common (Co) ($< 20 - 25$ years), and rare (Ra) (< 100 years) – and 2 thresholds for intensities – considerable (Co) and extreme (Ex). Intensity thresholds (Table 1) are chosen similarly to the types of hazards, with additional guidance that: 1. Each hazard should be present over a large geographical distribution at considerable intensity, but not everywhere; 2. Each hazard should have a different extent at higher intensity than lower intensity for all return periods; and 3. The intensities should be in line with very broad and cross-disciplinary intuitions about their potential impacts. The latter is very difficult to define, as impacts depend not only on the intensity of the hazard but also on the vulnerability of the affected system in question, which is not explicitly considered here. This varies very much between regions and systems, and consequently, the intensity thresholds are not to be understood directly as impact indicators. This is to be able to identify regions with similar hazard profiles but potentially very different impacts to guide research to understand these differences and system vulnerabilities or resilience. Importantly, the intensities are all defined in absolute terms and not as pure statistical anomalies such as, e.g., the 95th percentile of the lowest temperature per grid cell. This is central to our design because anomalies are incongruous with the definition of return periods. Hence, to have globally consistent, comparable, and time-resolved hazomes, we must employ absolute intensity definitions. Here, we caution readers who are used to thinking in terms of local, relative terms against drawing conclusions that might contrast with their acquired knowledge and intuition.

We remark that initially we tried to consider both intensities and return periods as continuous variables and to employ pattern recognition algorithms to identify geographical clusters of similar hazard profiles. Most attempts converged to the definition of clusters around hazard types and were very unstable. Thus, we decided to simplify the approach and fix thresholds for intensities and return periods to define the hazard profiles on which we build the hazomes.

In summary, in our definition of hazomes, therefore, choices had to be made, as in any classification task. These choices are qualitatively justified with regard to the purpose of hazomes: to be globally consistent, generically relevant for human and natural systems, based on freely available datasets, and to describe a system disturbance perspective. The latter requires the inclusion of both the intensity dimension and the temporal dimension of natural hazards. The choice of hazard

Table 1: Hazard variables. considerable and extreme intensity thresholds, as well as regular, uncommon, and rare return periods thresholds. The return periods are defined as the probability of occurrence per year for all hazards except earthquakes, for which we use the more common definition of 10% probability in 50 years. The intensity of the hazards are defined as the the 3-hour accumulated rain [mm] for heavy precipitations (HP), the Peak-Ground-Acceleration (PGA) in units of the gravitational acceleration on Earth g [$m s^{-2}$] for earthquakes (EQ), the 10-min sustained windspeed [$m s^{-1}$] for tropical cyclones (TC), the 3-day running average minimum temperatures for cold stress [$^{\circ}C$] (CS), the 3-day running average maximum Wet-Bulb-Globe [WGT] temperature [$^{\circ}C$] for heat stress (HS), the annual maximal depth [m] for flood (FL), the maximum monthly water deficit [mm column water equivalent] (WD), and the 95th percentile of the annual fire line intensity in mega-Watts for wildfires (WF). A grid cell is considered flooded if at least 2% of its area has a depth of at least 5 cm and a grid cell is considered a wildfire if at least 1% of its area is burnt in one season (Mar-Feb). The resulting spatial distributions of hazards are shown in the Supplementary Figures S11 - S14.

Categories	HP	EQ	TC	CS	HS	FL	WD	WF
Intensity unit	mm	g	$m s^{-1}$	$^{\circ}C$	$^{\circ}C$	m	mm	MW
Considerable (Co)	50	0.2	29	-25	30	0.3	125	100
Extreme (Ex)	125	0.4	43	-45	34	1.5	250	500
Regular (Re)	5	-	10	5	5	5	5	5
Uncommon (Un)	20	10%/ 50	20	20	20	25	20	20
Rare (Ra)	100	-	100	100	100	100	-	-

types strongly influences the results, and using others, such as volcanoes, landslides, winter storms, avalanches, or tsunamis, would result in more finely resolved hazomes. Additionally, the specific definition used for the chosen hazards, such as heatwaves in terms of consecutive days anomalies instead of heat stress as the maximum wet-bulb temperatures, would also alter the results. Below we provide detailed information on the data and chosen thresholds for each hazard type.

Hazome name coding convention In order to label hazomes, we employ the following coding convention: [Return period][Intensity][Hazard type]. In addition, for each hazard type, only the strongest intensity for the most frequent return period is listed. For the examples discussed in the manuscript, we obtain the following. The hazome in Zurich (Switzerland) is rare (Ra) considerable (Co) floods (FL) coupled with uncommon (Un) extreme (Ex) water deficits (WD), i.e., [RaCoFL, UnExWD], and in Bengaluru (India), regular (Re) considerable (Co) heavy precipitations (HP) are paired with regular (Re) considerable (Co) heat stress (HS) and regular (Re) extreme (Ex) water deficit (WD), i.e., [ReCoHp, ReCoHS, ReExWD]. A more complex hazome as in Seoul (South Korea) with regular considerable heavy precipitations, uncommon considerable tropical cyclones, rare considerable cold stress, regular considerable heat stress, uncommon considerable floods, and regular considerable water deficit reads [ReCoHP, UnCoTC, RaCoCS, ReCoHS, UnCoFL, ReCoWD]. Some places have twice the same hazard type at different intensity-return period combinations, such as rare considerable heavy precipitations, uncommon considerable cold stress, regular considerable water deficit and rare extreme water deficit in Obwalden (Switzerland) [RaCoHP, UnCoCS, ReCoWD, RaExWD].

Heavy precipitation For heavy precipitation data, we use Global Precipitation EXtremes (GPEX) (48). The data set contains global precipitation amounts in mm for several accumulation times (3, 6, 12, 24, 48, 72, 120, 240 hours) and several return periods (2, 5, 10, 20, 39, 50, 100, 200, 500, 1000 years). The values are linearly resampled from the original grid at 0.1° to the hazomes grid at 0.5° resolution. In general, daily and longer accumulation times are associated with fluvial flooding of large river systems (49), which are covered by the coastal and river flood data set. Shorter sub-daily accumulation times are related to flash floods, urban floods, or landslides triggers (50, 51, 52). Here, we thus choose the minimal accumulation time available in GPEX (i.e., of 3 hours).

GPEX is based on multi-Source Weighted-Ensemble Precipitation (MSWEP; (53)) dataset, which integrates data ranging from 1979 to 2017 from gauges, reanalysis, and satellites to provide global precipitation estimates. Although the MSWEP dataset offers high resolution (0.1°), spatial patterns can still be influenced by the density and distribution of gauge data, particularly in data-scarce regions; nevertheless, it has consistently proven to be a robust and valuable dataset for characterising precipitation extremes on the global scale (54). The precipitation return levels for different return periods in GPEX are estimated by fitting three types of extreme value distribution (GEV, POT, MEV). We use the Metastatistical Extreme Value (MEV; (55)) distribution, which is based on extreme value analysis of all precipitation events in the records (in contrast to an analysis based on annual maxima values), resulting in smoother and more consistent spatial estimates than the GEV and POT (peak-over-threshold) approaches and with reduced uncertainties in the estimates of precipitation extremes (56, 57). The 20- and 100-year return period thresholds defined for the uncommon and rare categories are rational, as they align with the return periods commonly used in the design of urban drainage systems and in planning measures to protect infrastructure from flood damage (58, 59). The considerable and extreme intensities of 50 and 125mm, respectively, roughly correspond to the flash flood warning and emergency flash floods warning thresholds for many European meteorological services.

Heat stress For heat stress return periods, we use the datasets provided by the World Bank, which include estimates for return periods of 5, 20, and 100 years. The methodology applies a generalised extreme value (GEV) distribution to model annual maximum Wet Bulb Globe Temperature (WBGT) extremes.

The data set is based on 30 years (1981–2010) of daily WBGT values, from which a three-day running mean is calculated to account for the cumulative effects of prolonged heat exposure. The annual maximum of these smoothed WBGT values is extracted for each grid cell and used to fit a GEV distribution via maximum likelihood estimation. The fitted distributions are then used to estimate return period thresholds for extreme heat events. To ensure numerical stability and reliability, flagged grid cells with unreliable estimates were adjusted by modifying the GEV fitting tolerance.

According to the ISO 7243 Heat Stress Standard, the considerable thresholds of 30C° correspond to the limit for continuous light work (60). The extreme threshold of 34C° typically exceeds the recommended limits for most sustained activity and often corresponds to a severe weather warning threshold with a high probability of heat illness unless exposure is curtailed (61).

Tropical cyclones For tropical cyclones, we use the STORM dataset (version 4) (62). The data set is openly available and provides global gridded wind speed intensities for a wide range of return

periods from 10 to 10,000 years. The data is based on the STORM (Synthetic Tropical cyclone Generation Model) model (63), which derives synthetic tropical cyclone tracks based on inputs from the International Best Track Archive for Climate Stewardship (IBTrACS) for 10,000 years of tropical cyclone activity under current climate conditions (reference period 1980-2017). Bloemendaal et al. apply a 2D parametric wind model to the synthetic tracks to estimate wind speed intensities for different return periods ("fixed return periods") and vice versa ("fixed intensity data"). We used the "fixed return periods" dataset, which contains the mean wind speed at the given return period as 10-metre 10-minute sustained average values. Data are resampled from the original resolution of 10 km to the Hazomes grid at 0.5° using the maximum wind speed within each 0.5° grid cell. We used 10, 20, and 100-year return periods, while the considerable and extreme intensity categories are 29.0 and 43.4 m/s 10-minute average sustained wind speed, respectively, which corresponds to category 1 ("Very dangerous winds will produce some damage") and category 3 ("Devastating damage will occur"), respectively, on the Saffir-Simpson Hurricane Scale (64). Although extreme winds are only one of several sub-hazards of tropical cyclones, others, such as heavy precipitation and flooding, are (partially) covered in other datasets presented in this section.

Cold stress As no global data set on cold stress return periods was available, we developed one using a methodology similar to that applied to heat stress return periods. We used ERA5 daily minimum temperature data for the period 1990–2020 and computed a rolling mean of three days to account for the short-term persistence in cold events. For each point on the grid, we extracted the annual minimum value of this rolling mean. The GEV distribution was then fitted to these minima to estimate the cold stress return periods at 5, 20, and 100 years.

During this process, we identified unrealistic parameter estimates in some grid points. Specifically, some locations exhibited extreme cold temperature estimates below -100°C , which are physically implausible, or shape parameters (ξ) greater than 0.5, which can lead to unstable tail behaviour in the fitted distribution. To address these issues, we 1. capped the shape parameter at 0.5 to prevent excessively heavy-tailed distributions, and 2. when the estimated 1-in-100-years cold event fell below -100°C , we set the shape parameter at zero ($\xi = 0$), effectively applying a Gumbel distribution instead of a full GEV fit. These adjustments ensured numerical stability and improved the physical plausibility of the return period estimates.

Occupational safety adaptations such as OSHA's wind-chill guidelines indicate that around the considerable threshold of -25°C , exposed skin can freeze in an hour, while the extreme value -45°C represents an extreme danger that causes freezing in less than 30 seconds (65).

Coastal and river floods For floods, we used the coastal flood and river flood return period maps from the Aqueduct Floods tool (66). The methods used to develop these data generate flood return period maps that depict the extent and depth of flooding for various return periods (2, 5, 10, 25, 50, 100, 250, 500 and 1,000 years) at a resolution of 30 arcseconds (approximately 1 kilometre at the equator). Note that neither river nor coastal flood maps account for changes in land use, infrastructure development, or flood defence measures that may have occurred over time.

The method used to develop river flood hazard maps is described in (67, 68). The maps were developed within the Global Flood Risk with IMAGE Scenarios (GLOFRIS) framework. In brief, daily gridded discharge and flood volumes were simulated ($0.5^\circ \times 0.5^\circ$) using the PCR-GLOBWB-DynRout model (69), which requires daily gridded meteorological input data (precipitation, temper-

ature, global radiation). These forcing data were EU-WATCH data (70) for the period 1960-1999. From each of the daily gridded flood volume time series, the flood volumes for the aforementioned return periods were calculated by fitting a Gumbel distribution through the annual maxima, thus producing coarse resolution flood volume maps ($0.5^\circ \times 0.5^\circ$) for each return period. Then these were downscaled to 30 arcseconds using the method of (67).

For coastal floods, the Global Tide and Surge Reanalysis (GTSR) data set (71) is used to estimate extreme water levels, incorporating wind and pressure fields from the ECMWF Reanalysis-Interim Data Set (ERA-Interim) and tide simulations from the Finite Element Solution 2012 (FES 2012) model. The GTSR data set covers the period 1979 to 2014, providing a solid historical basis for assessing coastal flood hazards. The topographic data used in this process include the Hydrological Data and Maps Based on Shuttle Elevation Derivatives at Multiple Scales (HydroSHEDS) and the Global 30-Arc-Second Elevation (GTOPO30) datasets. For the calculation of the return period, a Gumbel distribution is fitted to the annual extremes. These return periods are then mapped using a volume spreading model for river floods and a GIS-based routine for coastal floods, providing a detailed representation of historical flood risks (72).

For each type of flood, we transform the original data into single intensity maps at a 0.5° resolution with a 3-step process: 1. We select data points with flood depth greater than a minimal value of $t = 0.05m$; 2. We compute the fraction of points within each 0.5° grid cell. If the fraction exceeds a threshold $f = 2\%$, we define the grid cell as flooded; and 3. For each flooded grid cell, the flood depth is obtained as the average depth on all data points above the minimal value t . The coastal and river flood maps are then combined into a single flood map per return period by taking the maximum flood depth per grid cell.

Note that the minimum area requirement and average depth definition lead to artefacts if the flooded area increases faster than the average depth when increasing the return period. For example, consider a grid cell which at return period of 20-years has a flooded fraction of 3% (the area with flood depth $> t = 0.05$) with an average depth over this fraction of $1.6m$. Then, at a 100-year return period, the flood is much larger, covering a fraction of 26% (the area with flood depth $> t = 0.05$), but at a lower average flood depth of $0.6m$. Thus, the grid cell would be of extreme intensity at 20-year return period ($> 1.5m$), but only of considerable intensity at a 100-year return period ($> 0.3m, < 1.5m$), which violates the cumulative definition of return periods. We corrected for these artefacts by increasing the intensity category of all grid cells having a lower intensity category at a longer return period than at a shorter return period. These corrections affect less than 2% of the land-flooded grid cells.

The considerable thresholds of $0.3m$ roughly correspond to the maximum safe wading depth for an adult. It is widely used as a practical threshold where walking or evacuation becomes noticeably harder and buildings begin to incur meaningful damage (73). Many depth–damage functions and guidelines treat $0.3m$ as the lower limit for (non-trivial) residential damage and roads that become unusable for normal traffic. The extreme threshold of $1.5m$ is a depth at which most adults cannot stand in still water, which represents a direct threat to life, and at which most buildings suffer serious damage (74).

Water deficit Water resources are central to many natural and human systems. Not only do flora, fauna, and people depend on it, but also agriculture, navigation on rivers, and energy production. Quantifying particular deviations presents itself as a challenging task, as the definition of system

boundaries is highly dependent on the impact of interest, and thus which hydrometeorological variables are best suited to identify deficits (see, e.g. (75) for an extensive list of drought indices).

We use deficits in total water storage (TWS), as TWS provides a combination of all hydro-meteorological variables (76). Using changes in the gravitational field, the GRACE Gravity Recovery and Climate Experiment estimates monthly changes in total water storage on a 3° grid (77, 78, 79). We use a downscaled version of this data set (0.5° , hazomes grid), which was generated using a deep learning algorithm and hydrological model simulations for the years 2002–2022 (80). To account for normal seasonal differences in water availability, we de-seasonalise the data by subtracting the mean per month and grid cell. The resulting excess or deficit of water is expressed in millimetres of water column equivalent. We then compute the water deficit for return periods of 5 and 20 years and choose the categories 125mm (orange category, Fig. 1 in reference (76)) and 250mm (red category, Fig. 1 in reference (76)).

Wildfire We base wildfire return periods on two data sets provided by the Moderate Resolution Imaging Spectroradiometer (MODIS) for 24 wildfire seasons between March 2001 and February 2025. This temporal aggregation is adapted from the State of Wildfires report (81). We used the monthly 500-metre MCD64A1 MODIS burnt area product (82) to calculate the seasonal fraction of the total burnt grid cell area per Hazome grid cell. Additionally, we use the fire radiative power (FRP) from the MODIS active fire location product (83). This data set is available on 1 km with several daily satellite overpasses. We compute the seasonal 95th percentile in FRP per Hazomes grid cell, which has previously been used to approximate the intensity of the fire line (84).

The FRP hazard data set is used to approximate intensities with return periods of 5 and 20 years. Although observational records are relatively short, we rely on them rather than modelled burnt area because they avoid key limitations of global coupled vegetation-fire models. Models such as those in the Fire Model Intercomparison Project (85, *FireMIP*) struggle to capture inter-annual variability and extremes (86), and their performance varies by region (87).

Analogously to floods, we apply a two-step process: First, we filter grid cells where the fraction of burnt area exceeds a threshold $f = 1\%$ and define these as affected by wildfires. Second, we use the two categories of 100 and 500MW to differentiate between considerable (cool–small fires, Table 1 in reference (84)) and extreme fires (intense–large fires, Table 1 in reference (84)).

Other datasets For climate zones, we used the Köppen-Geiger classification for climate (1991–2020) based on constrained projections of CMIP6 as calculated by Beck et al. (2023). For biomes and ecoregions, we use the data set provided by Dinerstein et al. (2017) (9). For the population, we used the Worldpop 2020 1km resolution (88) resampled by summation to the hazome grid. For country names and boundaries, we use the Natural Earth administrative region data set (89). The city datasets are taken from GeoNames (90) via the GitHub repository joelacus/world-cities (91).

Hazome metrics To analyse the hazomes distribution, we define two metrics. The diversity metric counts the number of different types of hazard in a hazome. The haz-score is the sum over all instances where the intensity of a hazard type at a given return period exceeds an intensity category threshold. The haz-score can be computed with a simplified formula using the following rules. The return period multiplier F has for rare (Ra) events a value of 1, for uncommon (Un) events a value of 2, as they are more frequent than rare events, and for regular (Re) events a value of 3, as they

are more frequent than rare and uncommon events. The intensity multiplier I has for considerable (Co) events a value of 1, and for extreme (Ex) events a value of 2 because they are more intense than considerable events. The score S_h per hazard type h is obtained as the product of the return period F_h and the intensity multiplier I_h for that hazard type. The haz-score per grid cell x is then the sum of all hazard type scores S_{hx}

$$S^x = \sum_h S_{hx} = \sum_h F_{hx} \cdot I_{hx}. \quad (1)$$

For example, [ReCoCS] has a score of $3 * 1 = 3$, because regular considerable events are more frequent than uncommon and rare events. [RaExCS] has a score of $1 * 2 = 2$ because extreme events are more intense than considerable events. [RaCoCS, RaCoTC] has a score of $1 * 1 + 1 * 1 = 2$ due to two types of hazards, [UnExCS, ReCoTC] has a score of $2 * 2 + 3 * 1 = 7$, and [ReCoHp, RaExCS, UnExHS] has a score of $3 * 1 + 1 * 2 + 2 * 2 = 9$. The theoretical maximum value is 44 (3 return periods x 2 intensity x 8 hazard types - 4 missing datasets). This highlights the severity (higher score for more frequent and intense hazards) and diversity (higher score for more different types of hazards) of the haz-score.

References and Notes

1. L. Gunderson, Ecological and Human Community Resilience in Response to Natural Disasters. *Ecology and Society* **15** (2) (2010), publisher: Resilience Alliance Inc., <https://www.jstor.org/stable/26268155>.
2. P. Cui, *et al.*, Scientific challenges of research on natural hazards and disaster risk. *Geography and Sustainability* **2** (3), 216–223 (2021), doi:10.1016/j.geosus.2021.09.001, <https://www.sciencedirect.com/science/article/pii/S2666683921000390>.
3. P. J. Ward, *et al.*, Invited perspectives: A research agenda towards disaster risk management pathways in multi-(hazard)-risk assessment. *Natural Hazards and Earth System Sciences* **22** (4), 1487–1497 (2022), publisher: Copernicus GmbH, doi:10.5194/nhess-22-1487-2022, <https://nhess.copernicus.org/articles/22/1487/2022/>.
4. J. Zscheischler, *et al.*, Future climate risk from compound events. *Nature Climate Change* **8**, 469–477 (2018), 00000 Accepted: 2018-06-22T12:22:55Z tex.ids: Zscheischler2018c number: 6 publisher: Nature Publ. Group, doi:10.1038/s41558-018-0156-3, <https://www.research-collection.ethz.ch/handle/20.500.11850/268481>.
5. U. N. O. for Disaster Risk Reduction (UNDRR), International Science Council (ISC), *UNDRR-ISC Hazard Information Profiles – 2025 Update*, Tech. rep., United Nations Office for Disaster Risk Reduction (2025), doi:<https://doi.org/10.24948/2025.05>, <https://council.science/publications/review-hazard-profiles/>.
6. G. Messori, *et al.*, Global Mapping of Concurrent Hazards and Impacts Associated With Climate Extremes Under Climate Change. *Earth's Future* **13** (6), e2025EF006325 (2025), eprint: <https://agupubs.onlinelibrary.wiley.com/doi/pdf/10.1029/2025EF006325>, doi:10.1029/2025EF006325, <https://onlinelibrary.wiley.com/doi/abs/10.1029/2025EF006325>.
7. A. v. Humboldt, Duke University. Library. Jantz Collection. German Americana, *Ansichten der Natur : mit wissenschaftlichen Erläuterungen* (Stuttgart : J.G. Cotta) (1849), <http://archive.org/details/ansichtendernatu00humb>.
8. H. E. Beck, *et al.*, High-resolution (1 km) Köppen-Geiger maps for 1901–2099 based on constrained CMIP6 projections. *Scientific Data* **10** (1), 724 (2023), publisher: Nature Publishing Group, doi:10.1038/s41597-023-02549-6, <https://www.nature.com/articles/s41597-023-02549-6>.
9. E. Dinerstein, *et al.*, An Ecoregion-Based Approach to Protecting Half the Terrestrial Realm. *BioScience* **67** (6), 534–545 (2017), doi:10.1093/biosci/bix014, <https://doi.org/10.1093/biosci/bix014>.
10. S. J. Quan, P. Bansal, A systematic review of GIS-based local climate zone mapping studies. *Building and Environment* **196**, 107791 (2021), doi:10.1016/j.buildenv.2021.107791, <https://www.sciencedirect.com/science/article/pii/S0360132321001980>.

11. A. Champreux, F. Saltré, W. Traylor, T. Hickler, C. J. A. Bradshaw, How to map biomes: Quantitative comparison and review of biome-mapping methods. *Ecological Monographs* **94** (3), e1615 (2024), [_eprint: https://esajournals.onlinelibrary.wiley.com/doi/pdf/10.1002/ecm.1615](https://esajournals.onlinelibrary.wiley.com/doi/pdf/10.1002/ecm.1615), doi:10.1002/ecm.1615, <https://onlinelibrary.wiley.com/doi/abs/10.1002/ecm.1615>.
12. J. Hunter, S. Franklin, S. Luxton, J. Loidi, Terrestrial biomes: a conceptual review. *Vegetation Classification and Survey* **2**, 73–85 (2021), publisher: Pensoft Publishers, doi:10.3897/VCS/2021/61463, <https://vcs.pensoft.net/article/61463/>.
13. W. D. Köppen, Wärmezonen der Erde, nach der Dauer der heissen, gemässigten und kalten Zeit und nach der Wirkung der Wärme auf die organische Welt betrachtet. **1**, 215–226 (1884).
14. R. Geiger, Klassifikation der Klimate nach W. Köppen, in *andolt-Börnstein – Zahlenwerte und Funktionen aus Physik, Chemie, Astronomie, Geophysik und Technik* (Springer), vol. 3, pp. 603–607 (1954).
15. S. I. Higgins, R. Buitenwerf, G. R. Moncrieff, Defining functional biomes and monitoring their change globally. *Global Change Biology* **22** (11), 3583–3593 (2016), [_eprint: https://onlinelibrary.wiley.com/doi/pdf/10.1111/gcb.13367](https://onlinelibrary.wiley.com/doi/pdf/10.1111/gcb.13367), doi:10.1111/gcb.13367, <https://onlinelibrary.wiley.com/doi/abs/10.1111/gcb.13367>.
16. J. R. Smith, J. N. Hendershot, N. Nova, G. C. Daily, The biogeography of ecoregions: Descriptive power across regions and taxa. *Journal of Biogeography* **47** (7), 1413–1426 (2020), [_eprint: https://onlinelibrary.wiley.com/doi/pdf/10.1111/jbi.13871](https://onlinelibrary.wiley.com/doi/pdf/10.1111/jbi.13871), doi:10.1111/jbi.13871, <https://onlinelibrary.wiley.com/doi/abs/10.1111/jbi.13871>.
17. T. R. Loveland, J. M. Merchant, Ecoregions and Ecoregionalization: Geographical and Ecological Perspectives. *Environmental Management* **34** (1), S1–S13 (2004), doi:10.1007/s00267-003-5181-x, <https://doi.org/10.1007/s00267-003-5181-x>.
18. J. G. Pausas, W. J. Bond, Humboldt and the reinvention of nature. *Journal of Ecology* **107** (3), 1031–1037 (2019), [_eprint: https://besjournals.onlinelibrary.wiley.com/doi/pdf/10.1111/1365-2745.13109](https://besjournals.onlinelibrary.wiley.com/doi/pdf/10.1111/1365-2745.13109), doi:10.1111/1365-2745.13109, <https://onlinelibrary.wiley.com/doi/abs/10.1111/1365-2745.13109>.
19. P. S. White, A. Jentsch, The Search for Generality in Studies of Disturbance and Ecosystem Dynamics, in *Progress in Botany: Genetics Physiology Systematics Ecology*, K. Esser, U. Lüttge, J. W. Kadereit, W. Beyschlag, Eds. (Springer, Berlin, Heidelberg), pp. 399–450 (2001), doi:10.1007/978-3-642-56849-7_17, https://doi.org/10.1007/978-3-642-56849-7_17.
20. A. Jentsch, A. von Heßberg, Disturbance Regimes and Climate Extremes of the Earth’s Vegetation Zones, in *Disturbance Ecology*, T. Wohlgemuth, A. Jentsch, R. Seidl, Eds. (Springer International Publishing, Cham), pp. 41–75 (2022), doi:10.1007/978-3-030-98756-5_3, https://doi.org/10.1007/978-3-030-98756-5_3.
21. Z. Stalhandske, *et al.*, Global assessment of population exposure to multiple climate-related hazards from 2003 to 2021: a retrospective analysis. *The Lancet Planetary Health* p. 101295

- (2025), doi:10.1016/j.lanplh.2025.101295, <https://www.sciencedirect.com/science/article/pii/S2542519625001731>.
22. Z. Stalhandske, *et al.*, Global multi-hazard risk assessment in a changing climate. *Scientific Reports* **14** (1), 5875 (2024), tex.ids= Stalhandske2023, Stalhandske2023a publisher: Nature Publishing Group, doi:10.1038/s41598-024-55775-2, <https://www.nature.com/articles/s41598-024-55775-2>.
 23. J. N. Claassen, *et al.*, A new method to compile global multi-hazard event sets. *Scientific Reports* **13** (1), 13808 (2023), publisher: Nature Publishing Group, doi:10.1038/s41598-023-40400-5, <https://www.nature.com/articles/s41598-023-40400-5>.
 24. N. N. Ridder, *et al.*, Global hotspots for the occurrence of compound events. *Nature Communications* **11** (1), 5956 (2020), publisher: Nature Publishing Group, doi:10.1038/s41467-020-19639-3, <https://www.nature.com/articles/s41467-020-19639-3>.
 25. A. Bastos, *et al.*, A joint framework for studying compound ecoclimatic events. *Nature Reviews Earth & Environment* **4** (5), 333–350 (2023), tex.ids= Bastos2023a number: 5 publisher: Nature Publishing Group, doi:10.1038/s43017-023-00410-3, <https://www.nature.com/articles/s43017-023-00410-3>.
 26. M. Leonard, *et al.*, A compound event framework for understanding extreme impacts. *Wiley Interdisciplinary Reviews: Climate Change* **5** (1), 113–128 (2014), 00000 Publisher: John Wiley & Sons, Ltd, doi:10.1002/wcc.252, <https://onlinelibrary.wiley.com/doi/10.1002/wcc.252>.
 27. J. C. Gill, B. D. Malamud, Hazard interactions and interaction networks (cascades) within multi-hazard methodologies. *Earth System Dynamics* **7** (3), 659–679 (2016), tex.ids= Gill2016a publisher: Copernicus GmbH, doi:10.5194/esd-7-659-2016, <https://esd.copernicus.org/articles/7/659/2016/esd-7-659-2016.html>.
 28. C. on Safety criteria for dams, *Safety of Dams: Flood and Earthquake Criteria* (National Academies Press, Washington, D.C.) (1985), doi:10.17226/288, <http://www.nap.edu/catalog/288>.
 29. L. H. Comas, S. R. Becker, V. M. V. Cruz, P. F. Byrne, D. A. Dierig, Root traits contributing to plant productivity under drought. *Frontiers in Plant Science* **4**, 442 (2013), doi:10.3389/fpls.2013.00442.
 30. L. Berrang-Ford, *et al.*, A Systematic Global Stocktake of Evidence on Human Adaptation to Climate Change pp. 1–12, doi:10.1038/s41558-021-01170-y.
 31. M. Armon, Y. Shmilovitz, E. Dente, Anatomy of a foreseeable disaster: Lessons from the 2023 dam-breaching flood in Derna, Libya. *Science Advances* **11** (13), eadu2865 (2025), publisher: American Association for the Advancement of Science, doi:10.1126/sciadv.adu2865, <https://www.science.org/doi/abs/10.1126/sciadv.adu2865>.

32. Intergovernmental Panel On Climate Change (Ippc), *Climate Change 2021 – The Physical Science Basis: Working Group I Contribution to the Sixth Assessment Report of the Intergovernmental Panel on Climate Change* (Cambridge University Press), 1 ed. (2023), doi:10.1017/9781009157896, <https://www.cambridge.org/core/product/identifier/9781009157896/type/book>.
33. UNDRR, *Sendai Framework for Disaster Risk Reduction 2015-2030*, Tech. rep., UNDRR (2015), <https://www.undrr.org/publication/sendai-framework-disaster-risk-reduction-2015-2030>.
34. N. C. Bronfman, P. C. Cisternas, P. B. Repetto, J. V. Castañeda, Natural disaster preparedness in a multi-hazard environment: Characterizing the sociodemographic profile of those better (worse) prepared. *PLOS ONE* **14** (4), e0214249 (2019), publisher: Public Library of Science, doi:10.1371/journal.pone.0214249, <https://journals.plos.org/plosone/article?id=10.1371/journal.pone.0214249>.
35. M. C. De Ruiter, *et al.*, The Asynergies of Structural Disaster Risk Reduction Measures: Comparing Floods and Earthquakes. *Earth's Future* **9** (1), e2020EF001531 (2021), doi:10.1029/2020EF001531, <https://agupubs.onlinelibrary.wiley.com/doi/10.1029/2020EF001531>.
36. V. Cologna, *et al.*, Extreme weather event attribution predicts climate policy support across the world. *Nature Climate Change* pp. 1–11 (2025), publisher: Nature Publishing Group, doi:10.1038/s41558-025-02372-4, <https://www.nature.com/articles/s41558-025-02372-4>.
37. V. Wattin Håkansson, *et al.*, Beyond single company climate risk disclosure: event-based physical risk reporting. *Environmental Research: Climate* **4** (3), 035014 (2025), publisher: IOP Publishing, doi:10.1088/2752-5295/adf912, <https://dx.doi.org/10.1088/2752-5295/adf912>.
38. D. . W. B. G. Washington, Sovereign Catastrophe Risk Pools (Vol. 2 of 2) : World Bank Technical Contribution to the G20 (English), <http://documents.worldbank.org/curated/en/837001502870999632>.
39. A. B. Leverkus, *et al.*, Environmental policies to cope with novel disturbance regimes—steps to address a world scientists’ warning to humanity. *Environmental Research Letters* **16** (2), 021003 (2021), publisher: IOP Publishing, doi:10.1088/1748-9326/abdc5a, <https://dx.doi.org/10.1088/1748-9326/abdc5a>.
40. L. N. Svejcar, K. W. Davies, A. L. Ritchie, Ecological restoration in the age of apocalypse. *Global Change Biology* **29** (17), 4706–4710 (2023), eprint: <https://onlinelibrary.wiley.com/doi/pdf/10.1111/gcb.16809>, doi:10.1111/gcb.16809, <https://onlinelibrary.wiley.com/doi/abs/10.1111/gcb.16809>.
41. S. Hülsen, L. E. Dee, C. M. Kropf, S. Meiler, D. N. Bresch, Mangroves and their services are at risk from tropical cyclones and sea level rise under climate change. *Communications Earth & Environment* **6** (1), 1–9 (2025), tex.ids= Hülsen2025a publisher: Nature Pub-

- lishing Group, doi:10.1038/s43247-025-02242-z, <https://www.nature.com/articles/s43247-025-02242-z>.
42. M. D. Hurteau, B. A. Hungate, G. W. Koch, Accounting for risk in valuing forest carbon offsets. *Carbon Balance and Management* **4** (1), 1 (2009), doi:10.1186/1750-0680-4-1, <https://doi.org/10.1186/1750-0680-4-1>.
 43. A. W. Dye, *et al.*, Carbon, climate, and natural disturbance: a review of mechanisms, challenges, and tools for understanding forest carbon stability in an uncertain future. *Carbon Balance and Management* **19** (1), 35 (2024), doi:10.1186/s13021-024-00282-0, <https://doi.org/10.1186/s13021-024-00282-0>.
 44. R. T. Paine, M. J. Tegner, E. A. Johnson, Compounded Perturbations Yield Ecological Surprises. *Ecosystems* **1** (6), 535–545 (1998), doi:10.1007/s100219900049, <https://doi.org/10.1007/s100219900049>.
 45. B. Buma, Disturbance interactions: characterization, prediction, and the potential for cascading effects. *Ecosphere* **6** (4), art70 (2015), eprint: <https://esajournals.onlinelibrary.wiley.com/doi/pdf/10.1890/ES15-00058.1>, doi: 10.1890/ES15-00058.1, <https://onlinelibrary.wiley.com/doi/abs/10.1890/ES15-00058.1>.
 46. C. M. Kropf, L. Vaterlaus, D. N. Bresch, L. Pellissier, Tropical cyclone risk for global ecosystems in a changing climate. *Nature Climate Change* pp. 1–9 (2025), publisher: Nature Publishing Group, doi:10.1038/s41558-024-02194-w, <https://www.nature.com/articles/s41558-024-02194-w>.
 47. N. Peleg, M. Koukoulou, F. Marra, A 2°C warming can double the frequency of extreme summer downpours in the Alps. *npj Climate and Atmospheric Science* **8** (1), 216 (2025), publisher: Nature Publishing Group, doi:10.1038/s41612-025-01081-1, <https://www.nature.com/articles/s41612-025-01081-1>.
 48. G. J. Gründemann, *et al.*, Extreme precipitation return levels for multiple durations on a global scale. *Journal of Hydrology* **621**, 129558 (2023), doi:10.1016/j.jhydrol.2023.129558, <https://www.sciencedirect.com/science/article/pii/S0022169423005000>.
 49. R. Merz, G. Blöschl, A process typology of regional floods. *Water Resources Research* **39** (12) (2003), eprint: <https://agupubs.onlinelibrary.wiley.com/doi/pdf/10.1029/2002WR001952>, doi:10.1029/2002WR001952, <https://onlinelibrary.wiley.com/doi/abs/10.1029/2002WR001952>.
 50. M. Borga, M. Stoffel, L. Marchi, F. Marra, M. Jakob, Hydrogeomorphic response to extreme rainfall in headwater systems: Flash floods and debris flows. *Journal of Hydrology* **518**, 194–205 (2014), doi:10.1016/j.jhydrol.2014.05.022, <https://www.sciencedirect.com/science/article/pii/S0022169414003862>.
 51. E. Leonarduzzi, P. Molnar, Deriving rainfall thresholds for landsliding at the regional scale: daily and hourly resolutions, normalisation, and antecedent rainfall. *Natural Hazards and*

- Earth System Sciences* **20** (11), 2905–2919 (2020), publisher: Copernicus GmbH, doi:10.5194/nhess-20-2905-2020, <https://nhess.copernicus.org/articles/20/2905/2020/>.
52. N. Peleg, *et al.*, A simple and robust approach for adapting design storms to assess climate-induced changes in flash flood hazard. *Advances in Water Resources* **193**, 104823 (2024), doi:10.1016/j.advwatres.2024.104823, <https://www.sciencedirect.com/science/article/pii/S0309170824002100>.
 53. H. E. Beck, *et al.*, MSWEP V2 Global 3-Hourly 0.1° Precipitation: Methodology and Quantitative Assessment. *Bulletin of the American Meteorological Society* **100** (3), 473–500 (2019), publisher: American Meteorological Society Section: Bulletin of the American Meteorological Society, doi:10.1175/BAMS-D-17-0138.1, <https://journals.ametsoc.org/view/journals/bams/100/3/bams-d-17-0138.1.xml>.
 54. C. R. Rajulapati, *et al.*, Assessment of Extremes in Global Precipitation Products: How Reliable Are They? *Journal of Hydrometeorology* **21** (12), 2855–2873 (2020), publisher: American Meteorological Society Section: Journal of Hydrometeorology, doi:10.1175/JHM-D-20-0040.1, <https://journals.ametsoc.org/view/journals/hydr/21/12/jhm-d-20-0040.1.xml>.
 55. M. Marani, M. Ignaccolo, A metastatistical approach to rainfall extremes. *Advances in Water Resources* **79**, 121–126 (2015), tex.ids= Marani2015a, doi:10.1016/j.advwatres.2015.03.001, <https://www.sciencedirect.com/science/article/pii/S0309170815000494>.
 56. F. Marra, M. Koukoulas, A. Canale, N. Peleg, Predicting extreme sub-hourly precipitation intensification based on temperature shifts. *Hydrology and Earth System Sciences* **28** (2), 375–389 (2024), publisher: Copernicus GmbH, doi:10.5194/hess-28-375-2024, <https://hess.copernicus.org/articles/28/375/2024/>.
 57. F. Marra, E. I. Nikolopoulos, E. N. Anagnostou, E. Morin, Metastatistical Extreme Value analysis of hourly rainfall from short records: Estimation of high quantiles and impact of measurement errors. *Advances in Water Resources* **117**, 27–39 (2018), doi:10.1016/j.advwatres.2018.05.001, <https://www.sciencedirect.com/science/article/pii/S0309170818302033>.
 58. D. Butler, C. Dignam, C. Makropoulos, J. W. Davies, *Urban Drainage* (CRC Press, Boca Raton), 5 ed. (2024), doi:10.1201/9781003408635.
 59. P. Laux, *et al.*, Future precipitation extremes and urban flood risk assessment using a non-stationary and convection-permitting climate-hydrodynamic modeling framework. *Journal of Hydrology* **661**, 133607 (2025), doi:10.1016/j.jhydrol.2025.133607, <https://www.sciencedirect.com/science/article/pii/S002216942500945X>.
 60. K. Parsons, Heat Stress Standard ISO 7243 and its Global Application. *Industrial Health* **44** (3), 368–379 (2006), doi:10.2486/indhealth.44.368.

61. S.-C. C. Lung, J.-C. J. Yeh, J.-S. Hwang, Selecting Thresholds of Heat-Warning Systems with Substantial Enhancement of Essential Population Health Outcomes for Facilitating Implementation. *International Journal of Environmental Research and Public Health* **18** (18), 9506 (2021), doi:10.3390/ijerph18189506, <https://www.ncbi.nlm.nih.gov/pmc/articles/PMC8471601/>.
62. N. Bloemendaal, H. H. de Moel, S. Muis, I. I. Haigh, J. J. Aerts, STORM tropical cyclone wind speed return periods (2023), doi:10.4121/12705164.V4, <https://data.4tu.nl/datasets/0ea98bdd-5772-4da8-ae97-99735e891aff/4>.
63. N. Bloemendaal, *et al.*, Generation of a global synthetic tropical cyclone hazard dataset using STORM. *Scientific Data* **7** (1), 40 (2020), doi:10.1038/s41597-020-0381-2, <https://www.nature.com/articles/s41597-020-0381-2>.
64. National Hurricane Center, Saffir-Simpson Hurricane Wind Scale (2022), <https://www.nhc.noaa.gov/aboutsshws.php>.
65. U.S. Department of Labor Occupational Safety and Health Administration, The Cold Stress Equation (1998), https://www.ars.usda.gov/ARUserFiles/50620000/HealthandSafety/cold_stress.pdf?utm_source=chatgpt.com.
66. S. Kuzma, *et al.*, Aqueduct 4.0: Updated Decision-Relevant Global Water Risk Indicators (2023), <https://www.wri.org/research/aqueduct-40-updated-decision-relevant-global-water-risk-indicators>.
67. H. C. Winsemius, L. P. H. Van Beek, B. Jongman, P. J. Ward, A. Bouwman, A framework for global river flood risk assessments. *Hydrology and Earth System Sciences* **17** (5), 1871–1892 (2013), publisher: Copernicus GmbH, doi:10.5194/hess-17-1871-2013, <https://hess.copernicus.org/articles/17/1871/2013/hess-17-1871-2013.html>.
68. P. J. Ward, *et al.*, Assessing flood risk at the global scale: model setup, results, and sensitivity. *Environmental Research Letters* **8** (4), 044019 (2013), publisher: IOP Publishing, doi:10.1088/1748-9326/8/4/044019, <https://dx.doi.org/10.1088/1748-9326/8/4/044019>.
69. L. P. H. van Beek, Y. Wada, M. F. P. Bierkens, Global monthly water stress: 1. Water balance and water availability. *Water Resources Research* **47** (7) (2011), _eprint: <https://agupubs.onlinelibrary.wiley.com/doi/pdf/10.1029/2010WR009791>, doi:10.1029/2010WR009791, <https://onlinelibrary.wiley.com/doi/abs/10.1029/2010WR009791>.
70. G. P. Weedon, *et al.*, Creation of the WATCH Forcing Data and Its Use to Assess Global and Regional Reference Crop Evaporation over Land during the Twentieth Century. *Journal of Hydrometeorology* **12** (5), 823–848 (2011), publisher: American Meteorological Society Section: Journal of Hydrometeorology, doi:10.1175/2011JHM1369.1, https://journals.ametsoc.org/view/journals/hydr/12/5/2011jhm1369_1.xml.

71. S. Muis, M. Verlaan, H. C. Winsemius, J. C. J. H. Aerts, P. J. Ward, A global reanalysis of storm surges and extreme sea levels. *Nature Communications* **7** (1), 11969 (2016), publisher: Nature Publishing Group, doi:10.1038/ncomms11969, <https://www.nature.com/articles/ncomms11969>.
72. T. Tiggeloven, *et al.*, Global-scale benefit–cost analysis of coastal flood adaptation to different flood risk drivers using structural measures. *Natural Hazards and Earth System Sciences* **20** (4), 1025–1044 (2020), publisher: Copernicus GmbH, doi:10.5194/nhess-20-1025-2020, <https://nhess.copernicus.org/articles/20/1025/2020/>.
73. C. H. Aparicio Uribe, B. Russo, J. Téllez-Álvarez, E. Martínez-Gomariz, Flood-related hazard criteria during the human evacuation of underground spaces through stairs: a state-of-the-art review. *Natural Hazards* **121** (5), 5035–5073 (2025), doi:10.1007/s11069-024-07002-4, <https://doi.org/10.1007/s11069-024-07002-4>.
74. S. Jonkman, E. Penning-Rowsell, Human Instability in Flood Flows. *JAWRA Journal of the American Water Resources Association* **44** (5), 1208–1218 (2008), eprint: <https://onlinelibrary.wiley.com/doi/pdf/10.1111/j.1752-1688.2008.00217.x>, doi:10.1111/j.1752-1688.2008.00217.x, <https://onlinelibrary.wiley.com/doi/abs/10.1111/j.1752-1688.2008.00217.x>.
75. A. Toreti, *et al.*, World Drought Atlas (2024), iISBN: 9789268217887 9789268217894 ISSN: 1831-9424, 1018-5593, doi:doi:10.2760/3842670, <https://publications.jrc.ec.europa.eu/repository/handle/JRC139691>.
76. Y. Pokhrel, *et al.*, Global terrestrial water storage and drought severity under climate change. *Nature Climate Change* **11** (3), 226–233 (2021), doi:10.1038/s41558-020-00972-w, <https://www.nature.com/articles/s41558-020-00972-w>.
77. B. D. Tapley, S. Bettadpur, J. C. Ries, P. F. Thompson, M. M. Watkins, GRACE Measurements of Mass Variability in the Earth System. *Science* **305** (5683), 503–505 (2004), doi:10.1126/science.1099192, <https://www.science.org/doi/10.1126/science.1099192>.
78. J. Wahr, S. Swenson, V. Zlotnicki, I. Velicogna, Time-variable gravity from GRACE: First results. *Geophysical Research Letters* **31** (11), 2004GL019779 (2004), doi:10.1029/2004GL019779, <https://agupubs.onlinelibrary.wiley.com/doi/10.1029/2004GL019779>.
79. B. D. Tapley, S. Bettadpur, M. Watkins, C. Reigber, The gravity recovery and climate experiment: Mission overview and early results. *Geophysical Research Letters* **31** (9), 2004GL019920 (2004), doi:10.1029/2004GL019920, <https://agupubs.onlinelibrary.wiley.com/doi/10.1029/2004GL019920>.
80. J. Gou, B. Soja, Global high-resolution total water storage anomalies from self-supervised data assimilation using deep learning algorithms. *Nature Water* **2** (2), 139–150 (2024), doi:10.1038/s44221-024-00194-w, <https://www.nature.com/articles/s44221-024-00194-w>.

81. M. W. Jones, *et al.*, State of Wildfires 2023–2024. *Earth System Science Data* **16** (8), 3601–3685 (2024), doi:10.5194/essd-16-3601-2024, <https://essd.copernicus.org/articles/16/3601/2024/>.
82. L. Giglio, L. Boschetti, D. P. Roy, M. L. Humber, C. O. Justice, The Collection 6 MODIS burned area mapping algorithm and product. *Remote Sensing of Environment* **217**, 72–85 (2018), doi:10.1016/j.rse.2018.08.005, <https://linkinghub.elsevier.com/retrieve/pii/S0034425718303705>.
83. L. Giglio, W. Schroeder, C. O. Justice, The collection 6 MODIS active fire detection algorithm and fire products. *Remote Sensing of Environment* **178**, 31–41 (2016), doi:10.1016/j.rse.2016.02.054, <https://linkinghub.elsevier.com/retrieve/pii/S0034425716300827>.
84. S. Archibald, C. E. R. Lehmann, J. L. Gómez-Dans, R. A. Bradstock, Defining pyromes and global syndromes of fire regimes. *Proceedings of the National Academy of Sciences* **110** (16), 6442–6447 (2013), tex.ids= Archibald2013, Archibald2013a publisher: Proceedings of the National Academy of Sciences, doi:10.1073/pnas.1211466110, <https://pnas.org/doi/full/10.1073/pnas.1211466110>.
85. S. S. Rabin, *et al.*, The Fire Modeling Intercomparison Project (FireMIP), phase 1: experimental and analytical protocols with detailed model descriptions. *Geoscientific Model Development* **10** (3), 1175–1197 (2017), doi:10.5194/gmd-10-1175-2017, <https://gmd.copernicus.org/articles/10/1175/2017/>.
86. S. Hantson, *et al.*, Quantitative assessment of fire and vegetation properties in simulations with fire-enabled vegetation models from the Fire Model Intercomparison Project. *Geoscientific Model Development* **13** (7), 3299–3318 (2020), doi:10.5194/gmd-13-3299-2020, <https://gmd.copernicus.org/articles/13/3299/2020/>.
87. C. Burton, *et al.*, Global burned area increasingly explained by climate change. *Nature Climate Change* **14** (11), 1186–1192 (2024), doi:10.1038/s41558-024-02140-w, <https://www.nature.com/articles/s41558-024-02140-w>.
88. A. J. Tatem, WorldPop, open data for spatial demography. *Scientific Data* **4** (1), 170004 (2017), number: 1 Publisher: Nature Publishing Group, doi:10.1038/sdata.2017.4, <https://www.nature.com/articles/sdata20174>.
89. Natural Earth - Free vector and raster map data at 1:10m, 1:50m, and 1:110m scales, <https://www.naturalearthdata.com/>.
90. GeoNames, <https://www.geonames.org/>.
91. Joelacus, joelacus/world-cities (2025), <https://github.com/joelacus/world-cities>, original-date: 2023-10-17T01:27:52Z.
92. https://data.iac.ethz.ch/WCR_sandbox/Hazomes/hazome_maps.html.
93. A. Saltelli, ed., *Global sensitivity analysis: the primer* (John Wiley, Chichester, England ; Hoboken, NJ) (2008), oCLC: ocn180852094.

94. I. M. Sobol, Global sensitivity indices for nonlinear mathematical models and their Monte Carlo estimates. *Mathematics and Computers in Simulation* **55** (1), 271–280 (2001), tex.ids= Sobol2001, doi:10.1016/S0378-4754(00)00270-6, <https://www.sciencedirect.com/science/article/pii/S0378475400002706>.
95. J. Herman, W. Usher, SALib: An open-source Python library for Sensitivity Analysis. *Journal of Open Source Software* **2** (9), 97 (2017), doi:10.21105/joss.00097, <https://joss.theoj.org/papers/10.21105/joss.00097>.
96. C. M. Kropf, *et al.*, Uncertainty and sensitivity analysis for probabilistic weather and climate-risk modelling: an implementation in CLIMADA v.3.1.0. *Geoscientific Model Development* **15** (18), 7177–7201 (2022), doi:10.5194/gmd-15-7177-2022, <https://gmd.copernicus.org/articles/15/7177/2022/>.

Acknowledgments

The authors thank Nadia Bloemendaal, Maria Koroni, Benedikt Soja, Gou Junyang, Tyler L. McIntosh, and Kai Schröter for their valuable input during various discussions.

Funding: C.M.K. has received support from the European Union’s Horizon 2020 research and innovation programme grant agreement No 101003687 (PROVIDE), No 101073978 (DIRECTED), and No 101081369 (SPARCCLE). P.J.W. has received funding from the European Union’s Horizon 2020 research and innovation programme (MYRIAD-EU, grant agreement no. 101003276). N.P. has received support from the Swiss National Science Foundation (SNSF Grant number: 194649, “Rainfall and floods in future cities”). M.L.K.W has received support from the Dutch Sectorplan Bèta en Techniek, funded by the Ministry of OCW. C.B.S received funding from the Swiss Innovation Agency Innosuisse under Grant Agreement No 120.464 IP-SBM.

Author contributions: Conceptualization: C.M.K., C.B.S. S.H., Z.S., Methodology: C.M.K, C.B.S. S.H., Z.S., S.H., M.W., P.J.W., N.P., Formal analysis: C.M.K., Writing – Original Draft: C.M.K, C.B.S. S.H., Z.S., Writing – Review and Editing: C.M.K, C.B.S. S.H., Z.S., S.H., M.W., P.J.W., D.N.B., N.P., Visualisation: C.M.K

Competing interests: There are no competing interests to declare.

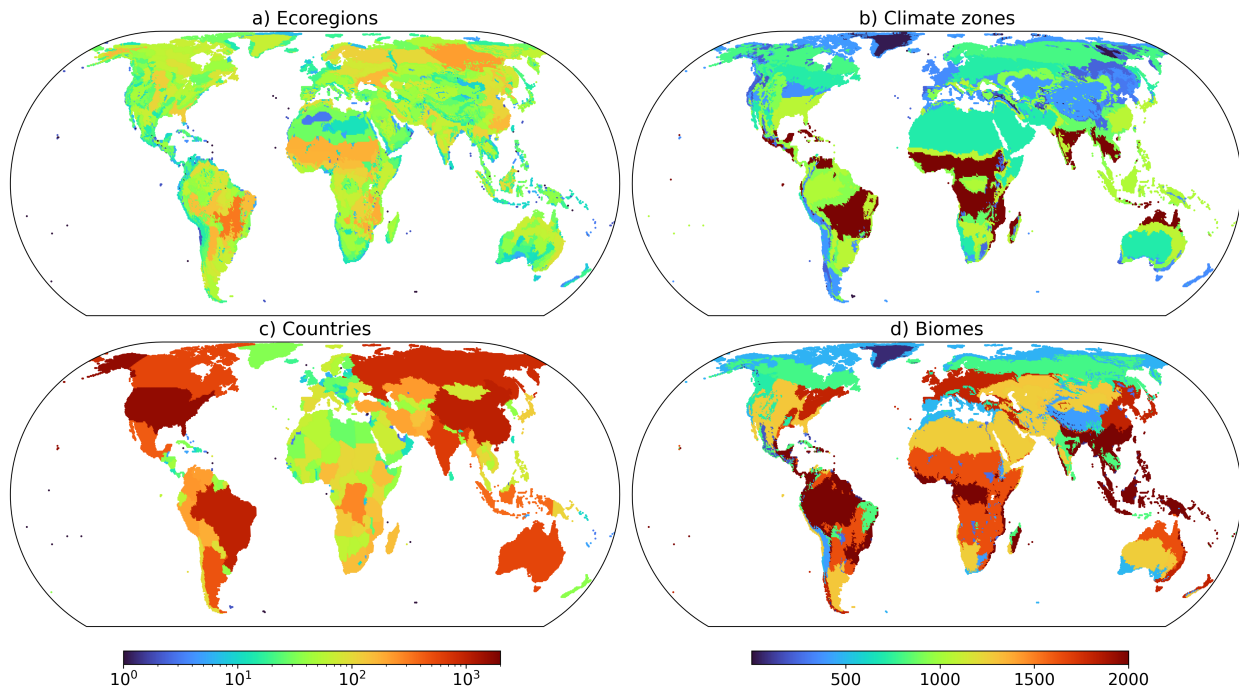
Data and materials availability: The main output data are available at (92). Upon publication, they will be deposited in a zenodo archive repository together with all the code. All input data sets are available open source from the providers as described in the Methods section 4.

5 Supplementary Text

5.1 Comparison to bio-climatic and societal classifications

The haz-score can be contrasted with bio-climatic and social classifications. In Figure S2, we show the median value for (a) ecoregions, (b) climate zones, (c) countries, and (d) biomes. The countries (administrative regions) with the highest median haz-score are Bangladesh, Taiwan and the Philippines ; the biomes with the highest score are Mangroves, Tropical & Subtropical Moist Broadleaf Forests, and Tropical & Subtropical Dry Broadleaf Forests ; the climate zones with the highest scores are Tropical rainforest; Tropical, monsoon; Tropical, savannah; Temperate, no dry season, hot summer; and Temperate, dry winter, hot summer ; and the highest-scoring ecoregions are Brahmaputra Valley semi-evergreen forests, Sundarbans freshwater swamp forests and the Sundarbans freshwater swamp forests. The top values are summarised in the supplementary table S2. In terms of human population distribution, we find that the majority (80% of the population lives at an intermediate score level between 4 – 15 out of the maximum of 23 (supplementary figure S7). Yet, the hazome with the highest population is the non-hazard hazome [], followed by [UnCoHp, ReCoHs], [UnCoWD], [UnCoHP, ReCoHS, UnCoWD] and [ReCoHP, RaExHP, UnCoEQ, ReExHS, ReCoFL, ReExWD] representing a diversity of combinations of hazard types, intensities, and return periods (Table S3).

Figure S1: Hazome variety comparison maps. Number of different hazomes per a) ecoregion, b) climatic zone, c) countries (administrative regions), and d) biomes. Please note the logarithmic colour scale on the left in a and c, and the linear colour scale on the right in b and d.



We further consider the number of distinct hazomes present per (a) ecoregion, (b) climate zones, (c) countries (administrative regions), and (d) biomes (Fig. S1). Generally, a larger area implies greater variety, in particular for countries which roughly follow a power-law area to hazome variety

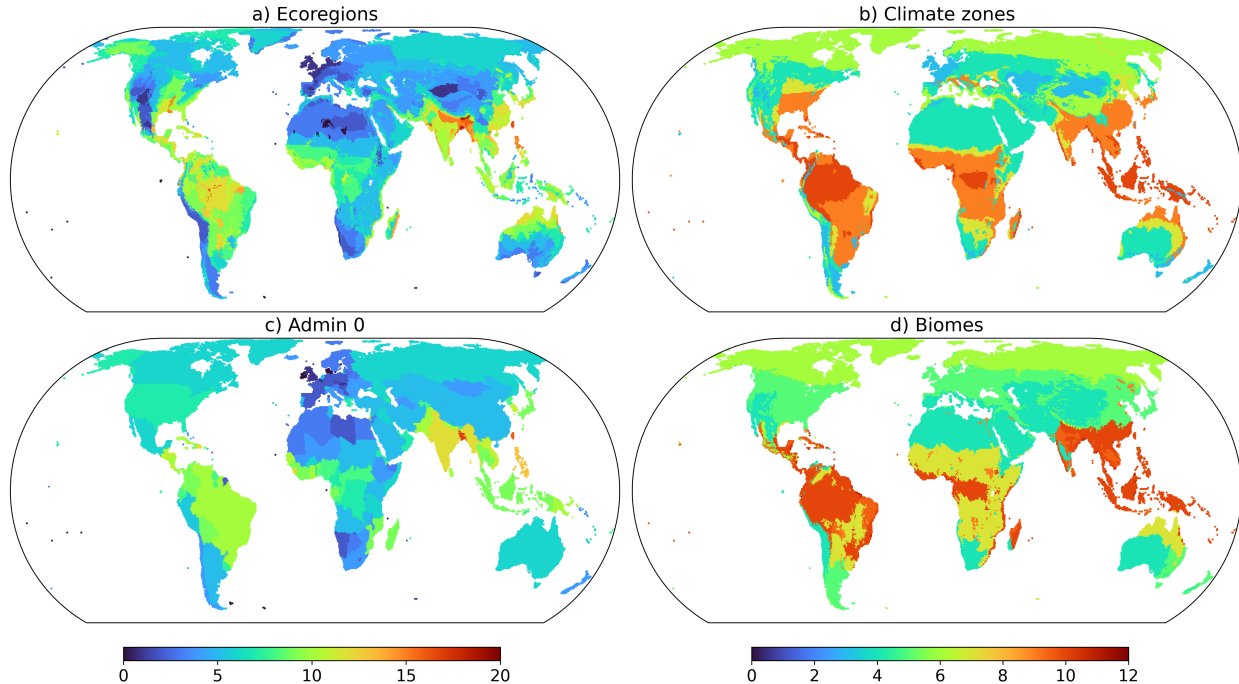


Figure S2: Haz-score comparison maps. Median haz-score per a) ecoregion, b) climatic zone, c) countries (administrative regions), and d) biome. The haz-score is obtained as the sum of all return periods and intensities for all hazards (see Fig. 2 and Methods 4 for details). Please note the different colour scales for plots a,c (maximum value 20) and b,d (maximum value 12). Interactive maps are available online for more detailed exploration.

distribution. For the climate zones, there are notable counter-examples, such as “Temperate, no dry season, hot summer”, which has the third largest number of different hazomes, while being only the eleventh largest out of 28. For biomes, Temperate Broadleaf & Mixed Forests (around the west-coast of North America, northern Europe and eastern Asia) and Tropical & Subtropical Moist Broadleaf Forests (around the Amazon basin, Congo basin, Indonesia and South-East Asia) show the highest diversity of hazomes, while for ecoregions, the East Siberian Taiga in Russia and the Cerrado in Brazil stand out with large diversity.

5.1.1 Sensitivity Analysis

We performed a sensitivity analysis on the hazomes classification to assess which hazard threshold choice leads to the largest changes in the output classification. Since the output is non-linear in the hazard thresholds, we perform a global sensitivity analysis (93) by varying all input threshold parameters at once. For each type of hazard, we vary the considerable and extreme intensity thresholds independently by 5% of the difference between the base values. In this way, the differences between the considerable and extreme thresholds vary by at most $\pm 10\%$. In addition, the depth and area threshold for the definitions of floods and wildfires are also varied by 5%. The values are then globally sampled from these ranges (see Table S1) with the Sobol sampling algorithm (94) for a total of 40959 samples. For each sample, the full hazomes are calculated. From this we derive the number of grid cells on land with a hazome different from the base and the total area of the changed

Table S1: Sensitivity analysis inputs. Uncertainty ranges for all thresholds used in the sensitivity analysis.

Categories	Co	Lower	Upper	Ex	Lower	Upper
HP (mm)	50	46.25	53.75	125	121.25	128.75
EQ (g)	0.2	0.19	0.21	0.4	0.39	0.41
TC (m/s)	29	28.3	29.7	43	42.3	43.7
CS (°C)	-25	-24	-26	-45	-44	-46
HS (°C)	30	29.8	30.2	34	33.8	34.2
FL (m)	0.3	0.24	0.36	1.5	1.44	1.56
WD (mm)	125	118.75	131.25	250	243.75	256.25
WF (kW)	100	80	120	500	480	520

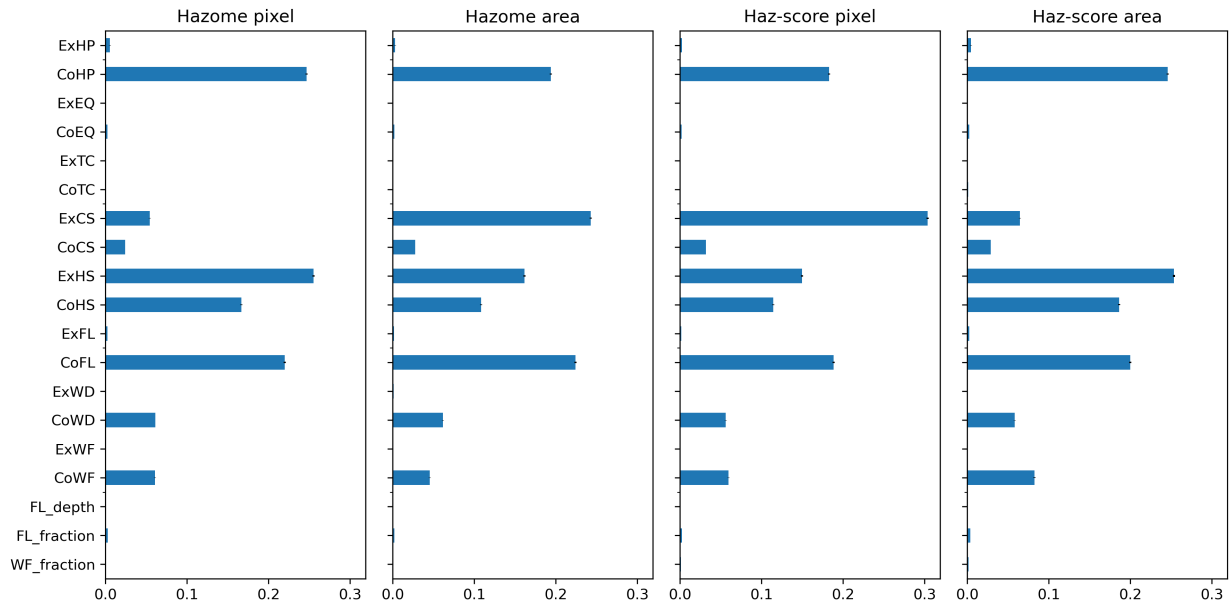
Categories	Base	Lower	Upper
WF minimal fraction	1%	0.95%	1.05%
FL minimal fraction	2%	1.9%	2.1%
FL flood depth threshold (cm)	0.05	0.0475	0.0525

grid cells. We further calculate the number of grid cells on land with a haz-score different from the base and the total area of the changed grid cells. Using the Saltelli algorithm (93) as implemented in the SALib Python library (95), the total first-order Sobol sensitivity indices, which capture the relative variance in the output due to the variance in each input, considering the second-order contributions of all other variables, are computed for each of the four outputs; see Figure S3. The confidence ranges from the Saltelli algorithm (see the bars in S3) are all smaller than the difference between sensitivity indices which are good indicators that the number of samples was sufficient for the analysis to converge (96).

We find that the hazomes pixel uncertainty is most sensitive to the intensity thresholds of the extreme heat stress (ExHS), considerable heavy precipitation (CoHP), considerable floods (CoFL) and considerable heat stress (CoHS). The uncertainty of the hazomes area is more sensitive to the intensity thresholds of extreme cold stress (ExCS), considerable floods (CoFL) and considerable heavy precipitation (CoHP). The haz-score pixel uncertainty is most sensitive to the intensity thresholds of extreme cold stress (ExCS), considerable heavy precipitation (CoHP), and considerable floods (CoFL). The haz-score area uncertainty is most sensitive to the intensity thresholds of extreme heat stress (ExHS), considerable heavy precipitation (CoHP), considerable floods (CoFL) and considerable heat stress (ExHS, CoHS). All metrics are insensitive to the intensity threshold for extreme heavy precipitation (ExHP), extreme and considerable earthquakes (CoEQ, ExEQ), extreme and considerable tropical cyclones (ExTC, CoTC), extreme floods (ExFL), extreme water deficit (ExWD), extreme wildfires (ExWF), as well as to the flood depth threshold, the flood minimum fraction, and the wildfire minimum fraction. Furthermore, all metrics are weakly sensitive to the intensity thresholds of considerable cold stress (CoCS), considerable water deficit (CoWD), and considerable wildfire (CoWF).

Note that sensitivity indices show how much of the output metric variance can be attributed to the input variable uncertainty. Hence, it does not indicate how large the variance in the output metric is. Moreover, the sensitivity is always strongly dependent on the definition of the uncertainty

Figure S3: Sensitivity indices. Sobol first-order total sensitivity indices ST if the inputs are varied within the bounds shown in table S1. Left: the ST for the total area change of the hazomes and of the haz-score. Right: the ST for the relative number of pixels that change their hazome and their haz-score. The black uncertainty bar indicating the confidence interval of the Saltelli algorithm are all smaller than the difference between sensitivity indices which shows that the number of samples was sufficient for convergence of the analysis.



ranges of the input variable.

Figure S4: Hazomes colours. Left: Visualization of the colour of all 8046 hazomes which arise from the additive mixing of the base colours for the hazard type, intensity and return period shown in the legend of Figure 1. The black pixels at the end are just filler and do not correspond to any hazome. Right: Visualization of the additive colour mixing for fifty randomly chosen hazomes with between two (left) and fifteen (right) base colours. For each large column, the last column corresponds to the mix of the row before. Note that the last columns are very pale.

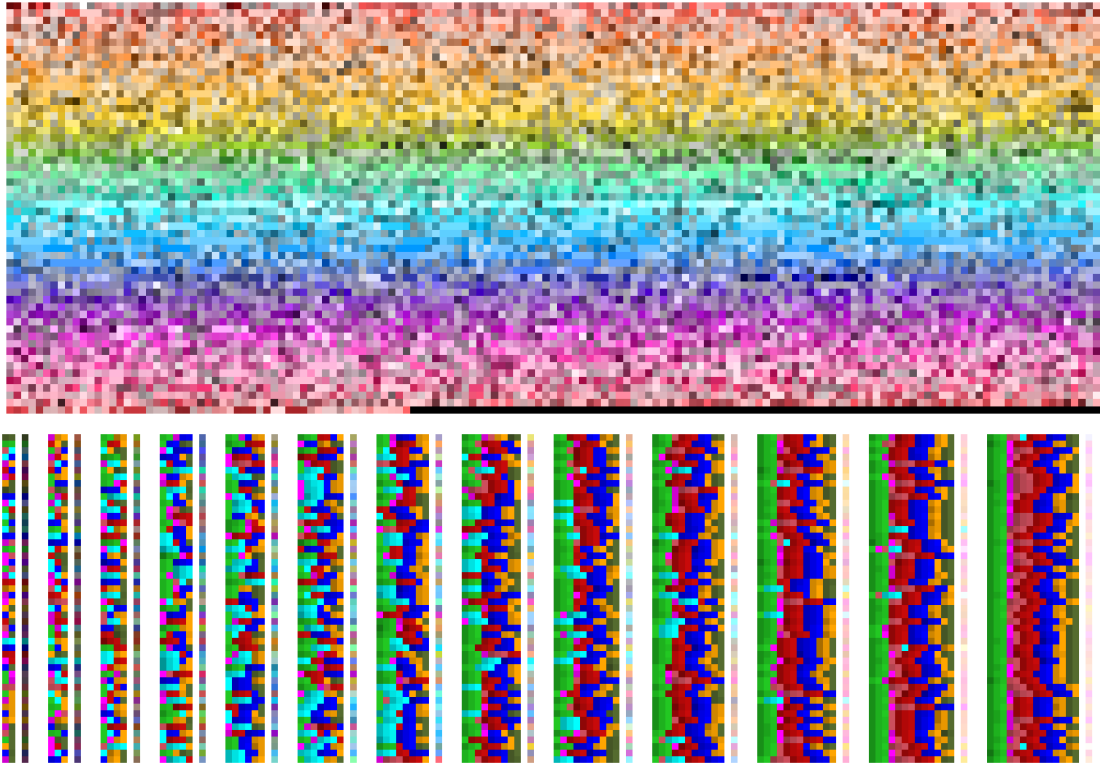


Figure S5: Hazome maps per hazard type. For each hazard type, the maps show the hazomes in which they are present for at least one intensity and return period threshold. The coloring is otherwise identical as for the full hazomes shown in Fig. 1. We find that all individual hazards are present across many hazomes, across longitudes, and across latitudes.

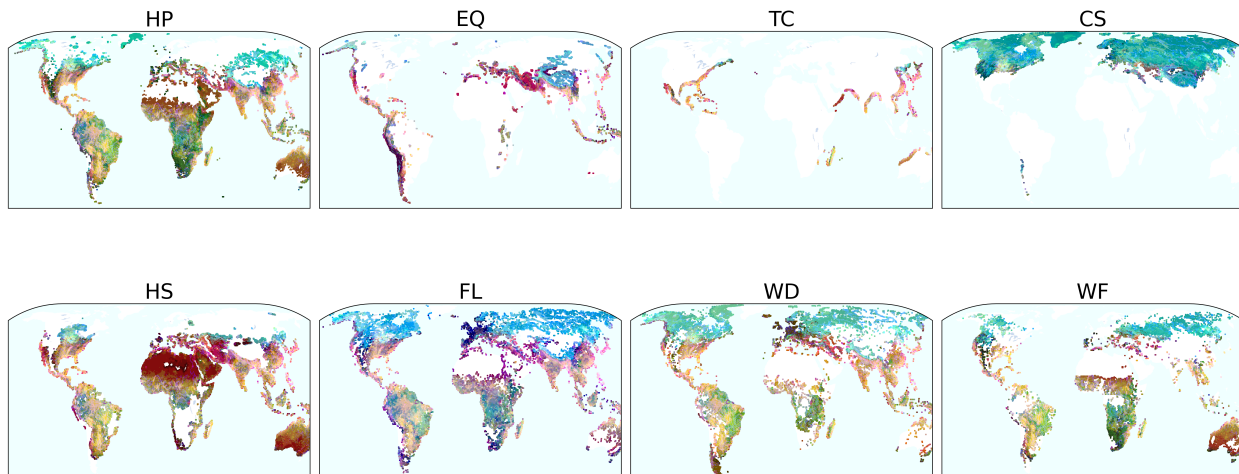


Figure S6: City twins with climate zones. Selection of cities with the corresponding most distant largest city above 5000 inhabitants with the same hazome that is at least 5 degrees distant shown overlayed on the Köppen-Geiger climate zones. Cities with the same color and marker have the same hazome. Cities with gray triangular markers (Tokyo, Tashkent, Antananarivo, Juba) are in a hazome that is unique in a radius of 5 degrees. Cities marked by circles have the same climate zones. Cities marked with squares, triangles, diamonds are in different climate zones. This figure is analog to Fig. 3.

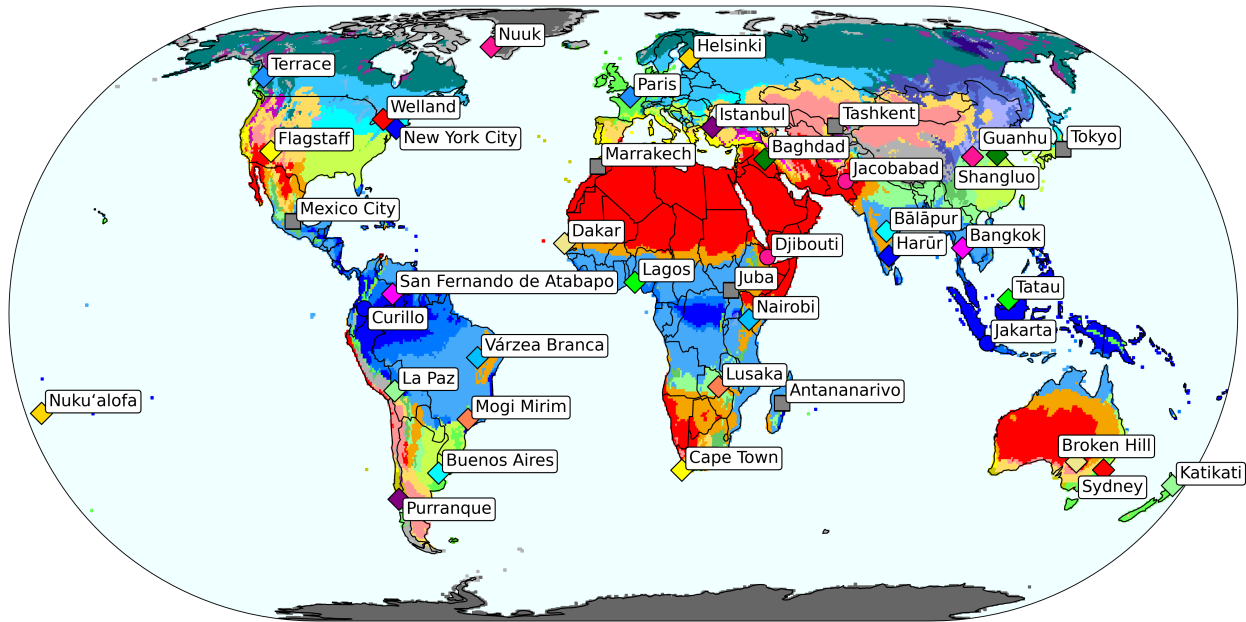


Figure S7: Population per hazome score. The majority of the world (80%) lives in regions with a haz-score between 4 and 15. Note the logarithmic y-axis.

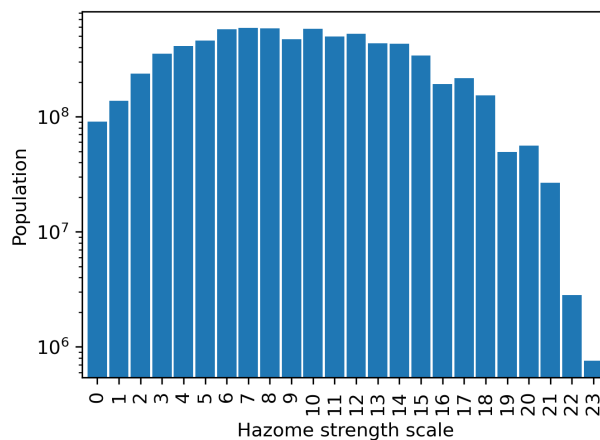


Table S2: Median haz-scores. Biomes, climate zones, ecoregions, and countries (administrative regions) with the largest median haz-score.

Country (administrative region)	Haz-score
Bangladesh	17
Taiwan	16
Philippines	13
The Gambia	12
Dominican Republic	12
India	12
Sierra Leone	12
Myanmar	12
Biome	Haz-score
Mangroves	11
Tropical & Subtropical Moist Broadleaf Forests	10
Tropical & Subtropical Dry Broadleaf Forests	9.5
Flooded Grasslands & Savannas	9
Tropical & Subtropical Grasslands, Savannas & Shrublands	7
Climatic zone	Haz-score
Tropical, rainforest	10
Tropical, monsoon	10
Tropical, savannah	9
Temperate, no dry season, hot summer	9
Temperate, no dry season, hot summer	9
Ecoregions	Haz-score
Brahmaputra Valley semi-evergreen forests	19
Sundarbans freshwater swamp forests	19
Sundarbans mangroves	18
Rann of Kutch seasonal salt marsh	17
Taiwan subtropical evergreen forests	16.5

Table S3: Hazomes area and population. Five largest hazomes and five most populous hazomes. For both the size and population, the largest hazomes is None, meaning without any hazard above the minimal intensity threshold for all return periods.

Hazome	Area (M km ²)	Population (M)
None	219.6	72.9
UnCoHP, ReCoHS	0.63	60.7
UnCoWD	0.52	48.2
UnCoHP, ReCoHS, UnCoWD	0.28	46.7
ReCoHP, RaExHP, UnCoEQ, ReExHS, ReCoFL, ReExWD	0.01	35.4

Figure S8: Heavy precipitation threshold map. Heavy precipitation intensity for all return periods with several thresholds (left) and the hazome threshold for considerable and extreme intensities (right). For each threshold category the percentage of land area affected is shown in parenthesis.

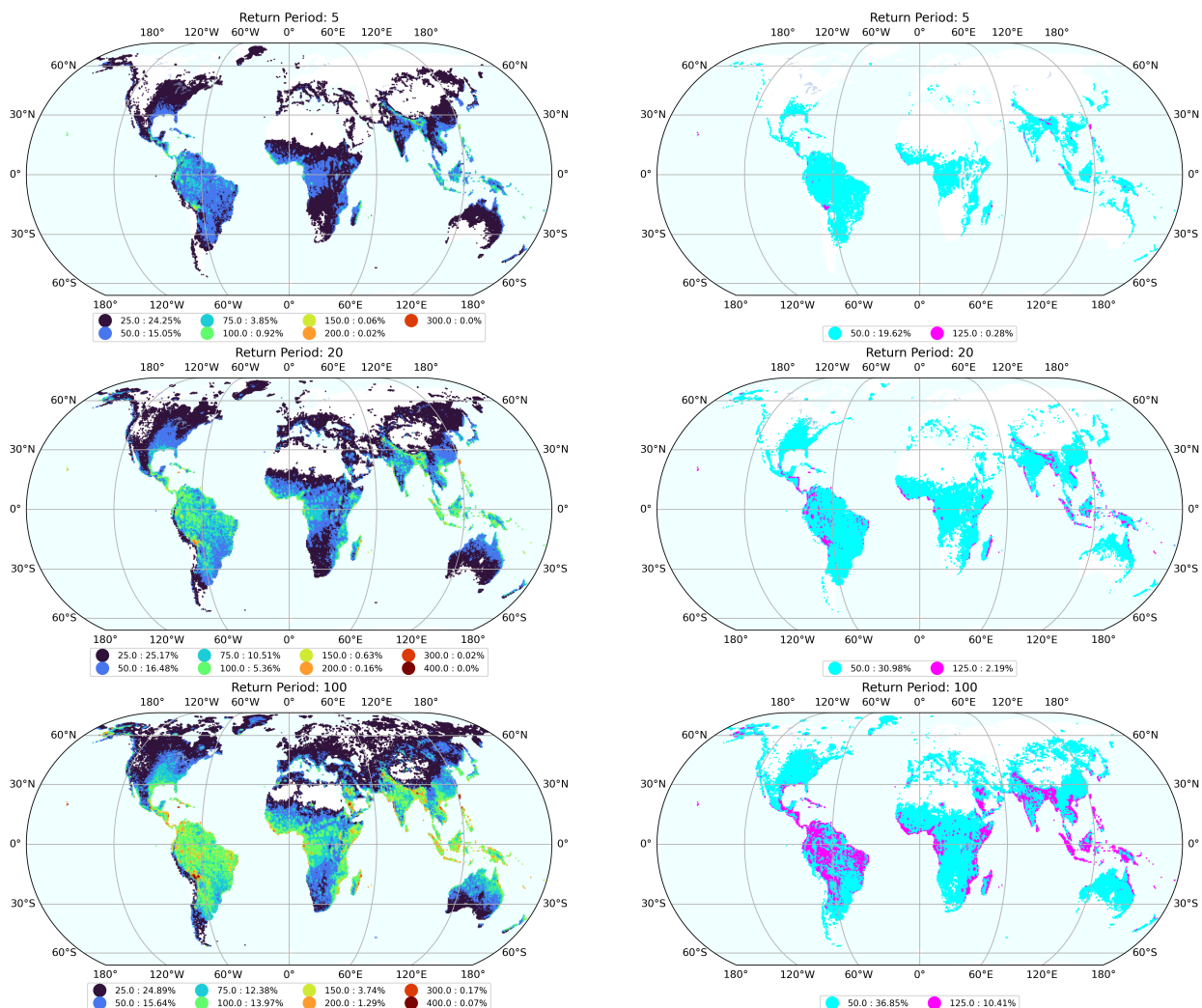


Figure S9: Earthquake threshold map. Earthquake intensity for all return periods with several thresholds (left) and the hazome threshold for considerable and extreme intensities (right). For each threshold category the percentage of land area affected is shown in parenthesis.

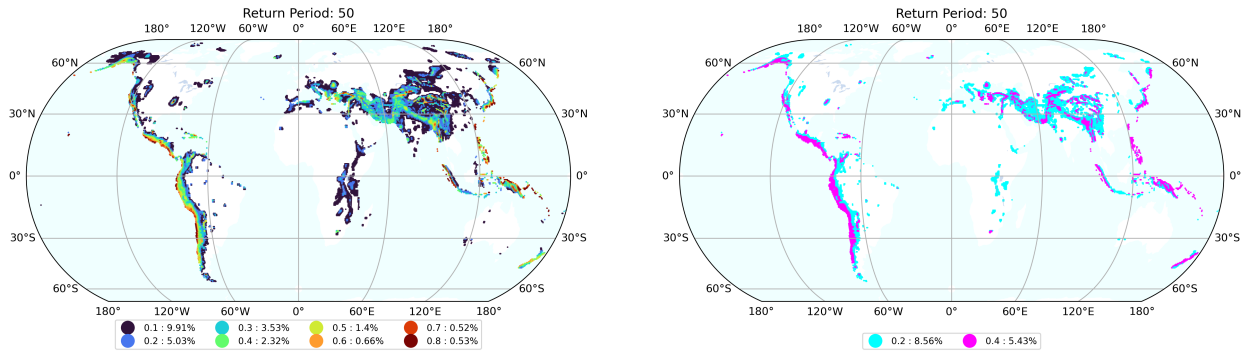


Figure S10: Tropical cyclones threshold map. Tropical cyclone intensity for all return periods with several thresholds (left) and the hazome threshold for considerable and extreme intensities (right). For each threshold category the percentage of land area affected is shown in parenthesis.

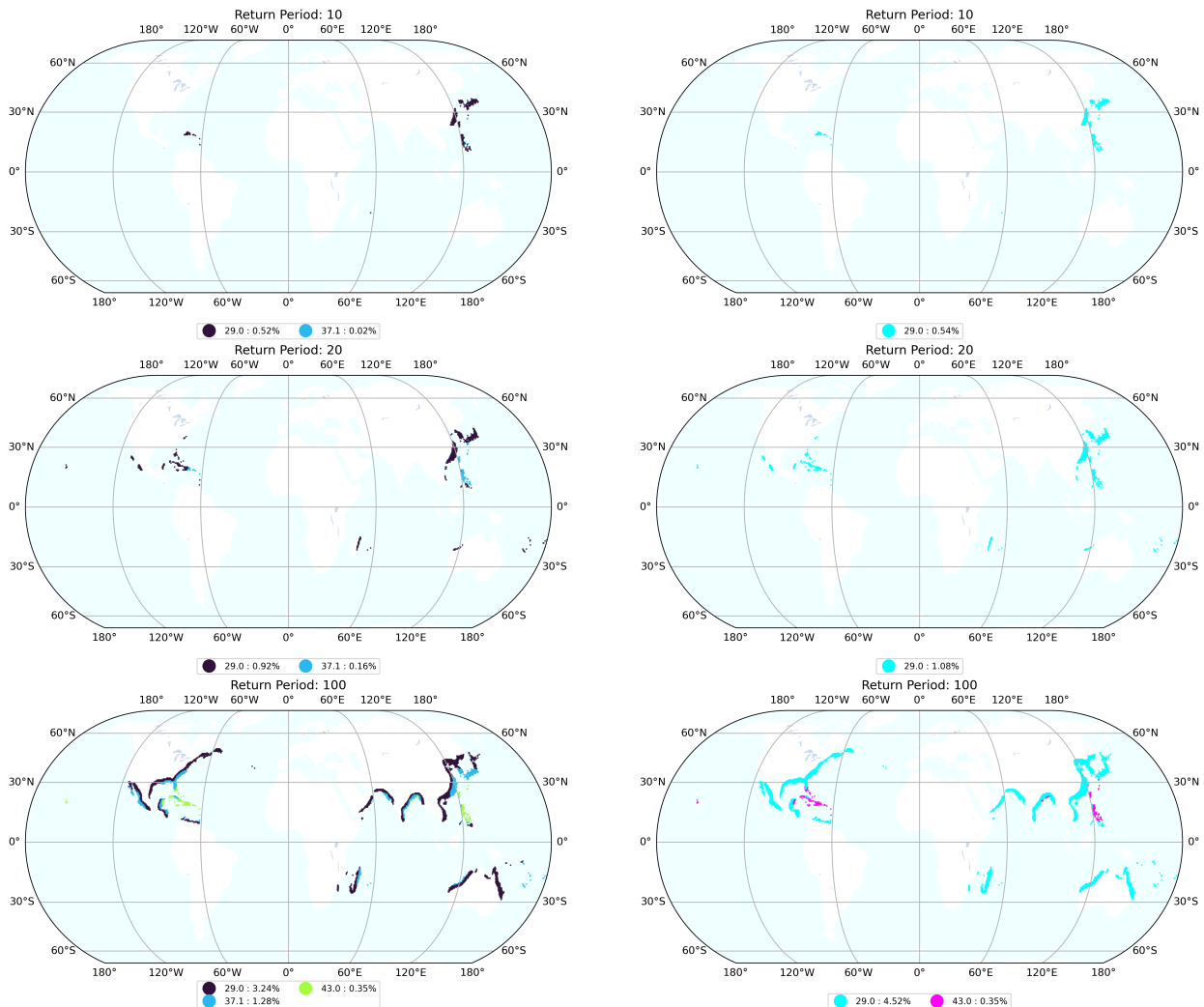


Figure S11: Cold stress threshold map. Cold stress intensity for all return periods with several thresholds (left) and the hazome threshold for considerable and extreme intensities (right). For each threshold category the percentage of land area affected is shown in parenthesis.

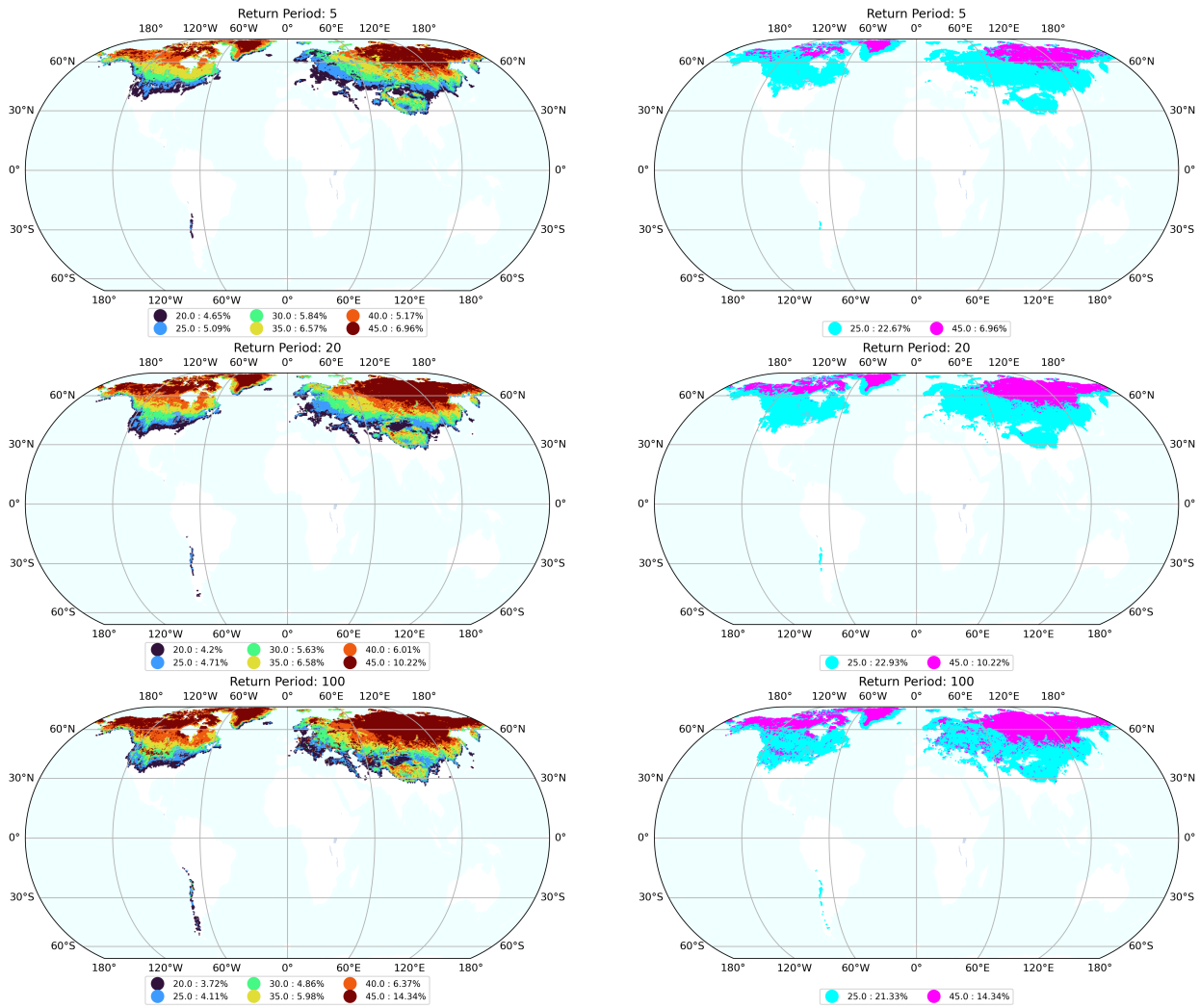


Figure S12: Heat stress threshold map. Heat stress intensity for all return periods with several thresholds (left) and the hazome threshold for considerable and extreme intensities (right). For each threshold category the percentage of land area affected is shown in parenthesis.

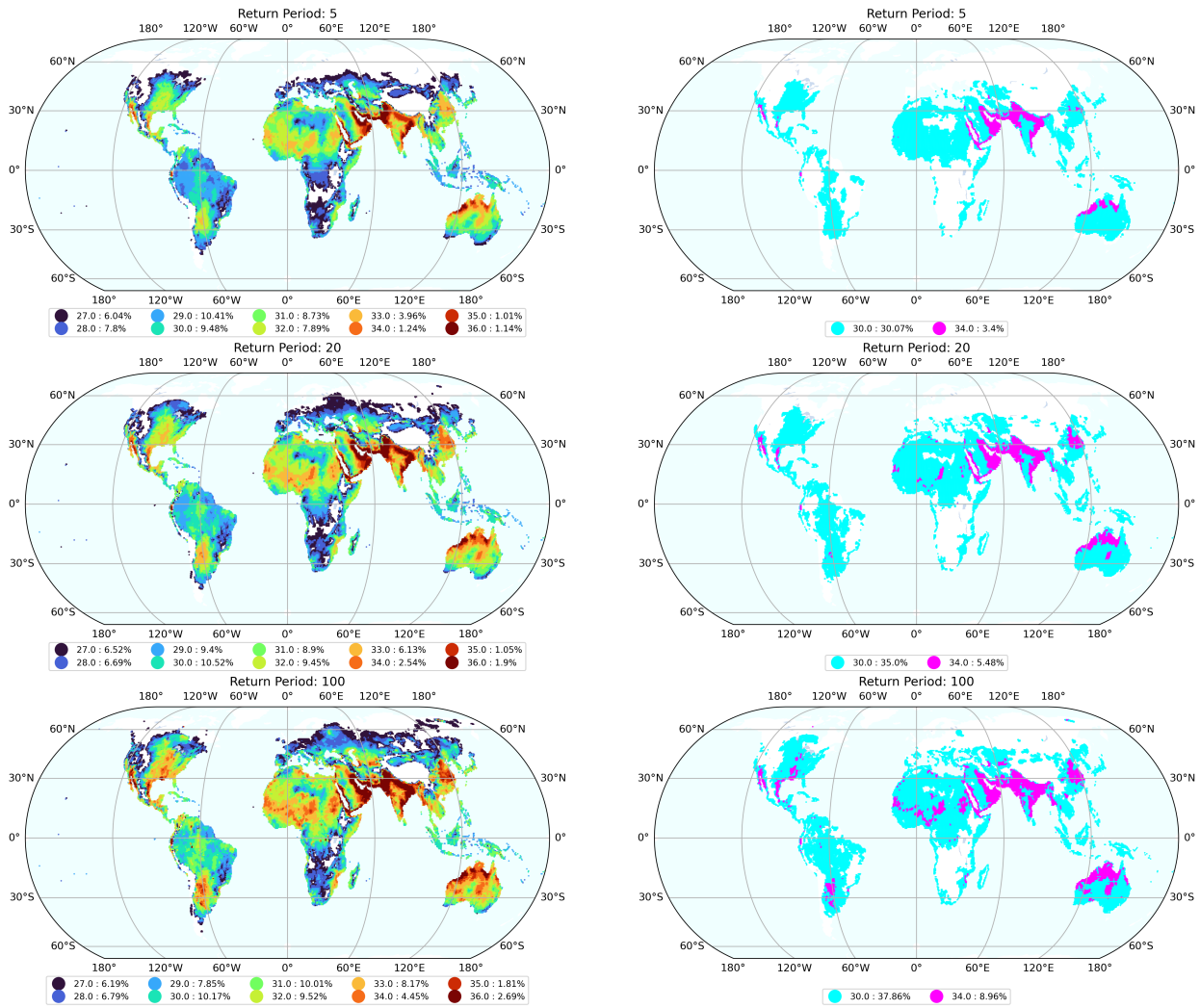


Figure S13: Flood threshold map. Flood intensity for all return periods with several thresholds (left) and the hazome threshold for considerable and extreme intensities (right). For each threshold category the percentage of land area affected is shown in parenthesis.

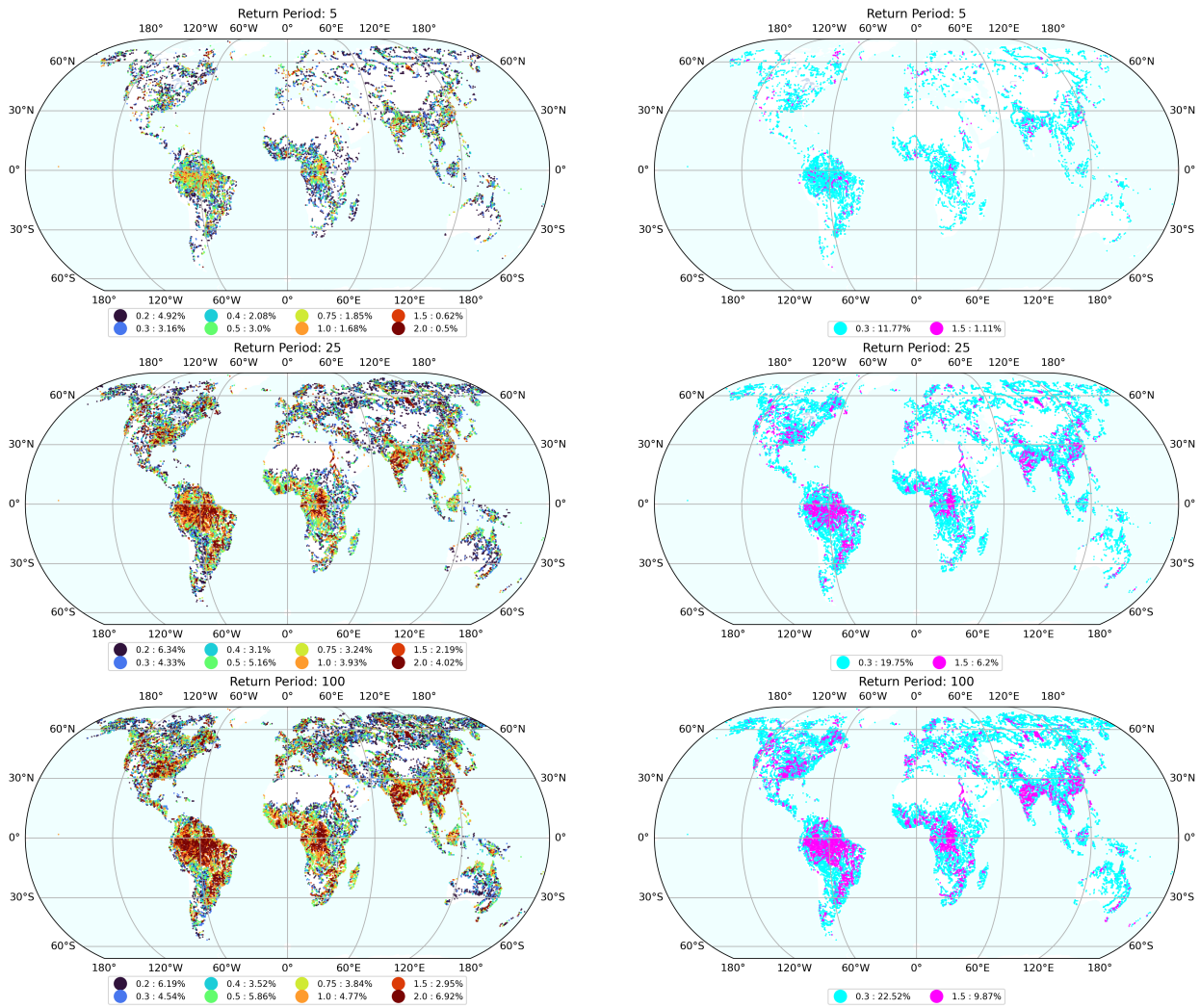


Figure S14: Water deficit threshold map. Water deficit intensity for all return periods with several thresholds (left) and the hazome threshold for considerable and extreme intensities (right). For each threshold category the percentage of land area affected is shown in parenthesis.

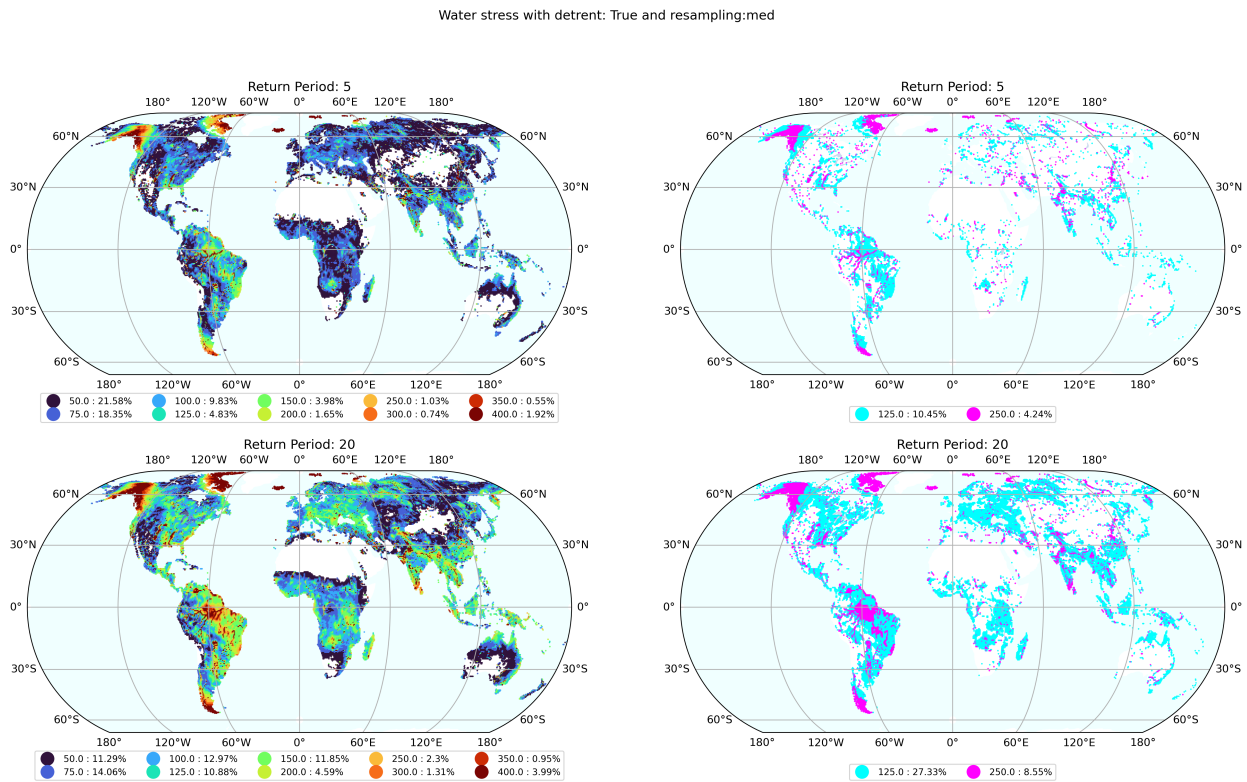


Figure S15: Wildfires threshold map. Wildfire intensity for all return periods with several thresholds (left) and the hazome threshold for considerable and extreme intensities (right). For each threshold category the percentage of land area affected is shown in parenthesis.

